Spectral characterisation of inertial particle clustering in turbulence

N. E. L. Haugen[1,2], A. Brandenburg[1,3], C. Sandin[1] and L. Mattsson[1]

[1]Nordita, KTH Royal Institute of Technology and Stockholm University, Hannes Alfvéns väg 12, SE-10691 Stockholm, Sweden

[2]SINTEF Energi A.S., Sem Saelands vei 11, 7034 Trondheim, Norway

[3]Department of Astronomy, Stockholm University, SE-10691 Stockholm, Sweden

(3 May 2021)

Clustering of inertial particles is important for many types of astrophysical and geophysical turbulence, but it has been studied predominately for incompressible flows. Here we study compressible flows and compare clustering in both compressively (irrotationally) and vortically (solenoidally) forced turbulence. Vortically and compressively forced flows are driven stochastically either by solenoidal waves or by circular expansion waves, respectively. For compressively forced flows, the power spectra of the density of inertial particles are a particularly sensitive tool for displaying particle clustering relative to the density enhancement. We use both Lagrangian and Eulerian descriptions for the particles. Particle clustering through shock interaction is found to be particularly prominent in turbulence driven by spherical expansion waves. It manifests itself through a double-peaked distribution of spectral power as a function of Stokes number. The two peaks are associated with two distinct clustering mechanisms; shock interaction for smaller Stokes numbers and the centrifugal sling effect for larger values. The clustering of inertial particles is associated with the formation of caustics. Such caustics can only be captured in the Lagrangian description, which allows us to assess the relative importance of caustics in vortically and irrotationally forced turbulence. We show that the statistical noise resulting from the limited number of particles in the Lagrangian description can be removed from the particle power spectra, allowing us a more detailed comparison of the residual spectra. We focus on the Epstein drag law relevant for rarefied gases, but show that our findings apply also to the usual Stokes drag.

Key words: particle/fluid flow, compressible flows, shock waves, compressible turbulence

1. Introduction

Turbulent gas flows often harbour particles of different sizes, for example dust grains or water droplets. Larger particles can have significant inertia and decouple from the flow. This can lead to local enhancements of their density, which is generally described as clustering. This can be important for the coalescence of particles to larger ones. This process eventually leads to the formation of planetesimals in planetary accretion discs (Weidenschilling 1980) or to raindrops in clouds (Shaw 2003; Grabowski & Wang 2013). Another situation where particle clustering is important is when reactive particles are "competing" for the same reactant gas. The concentration of reactant gas may then be

significantly lower within a particle cluster than outside, which yields an overall lower reaction rate (Krüger *et al.* 2017; Haugen *et al.* 2018; Karchniwy *et al.* 2019).

In clouds, and in most industrial applications, the compressibility of air is rather weak, because the turbulent flow speeds are strongly subsonic. This tends to be quite different in astrophysical flows such as those in accretion discs around young stars and the interstellar medium, which is continuously being fed with dust from the outflows of stars near the end of their lives. The driving of turbulence is fundamentally different in the meteorological and astrophysical contexts. Cloud turbulence is driven by convection, which is an intrinsically vortical flow. There is a large variety of turbulent industrial flows, but for the vast majority, the turbulence is typically driven by some sort of shear, which yields vortical flows. Turbulent flows with purely compressive driving are sometimes also referred to as acoustic (irrotational) turbulence or wave turbulence. Turbulence in the interstellar medium is driven predominately by supernova explosions, which are intrinsically compressive flows (see, e.g., Korpi *et al.* 1999; Mac Low & Klessen 2004; de Avillez & Breitschwerdt 2005; Federrath *et al.* 2011; Gent *et al.* 2013*a*,*b*, 2020; Evirgen *et al.* 2019). At larger flow speeds, however, vorticity can always be produced by baroclinicity and shocks (Federrath *et al.* 2011; Del Sordo & Brandenburg 2011; Porter *et al.* 2015).

To isolate the distinctive properties of compressive and vortical turbulence, we simulate isothermal turbulence by applying a stochastic forcing that is either vortical or compressive. In the latter case, the pressure enhancements, which are the result of energy injection of the forcing, are completely irrotational. It is only when the resulting spherical expansion waves interact with each other that some vorticity can be produced – especially for large Mach number, which is the ratio of root-mean-square (rms) velocity to the sound speed. Likewise, the purely vortical driving can lead to significant compression and finite flow divergences at larger Mach numbers (see, e.g., Federrath *et al.* 2011; Mattsson *et al.* 2019*a*).

For acoustic turbulence, the energy spectra drop slightly more rapidly with wavenumber k (like k^{-2}) compared to the $k^{-5/3}$ Kolmogorov spectrum for vortical turbulence (Kadomtsev & Petviashvili 1973). Acoustic turbulence does not necessarily imply large Mach numbers, because the bulk speed may well be less than the wave speed. Our primary interest lies in the clustering of particles in these two types of flows for small and large Mach numbers.

There are two rather different approaches to simulating non-interacting inertial particles. One is to model them as a pressure-less fluid, and the other is to model them as non-interacting point particles. In both cases, the particles interact with the gas through friction. We refer to these two approaches as Eulerian and Lagrangian, respectively. Each of them has advantages and disadvantages. A Lagrangian description is ideal for dilute systems, but it is susceptible to statistical noise, especially at small length scales where there are fewer particles. This is a disadvantage of the Lagrangian approach. An important disadvantage of the fluid description is that it cannot describe how particles of the same type can go past each other. This is because in the fluid description one only considers the bulk flow, which is the average velocity of all particles of a specific type in a small local volume. The bulk velocity is therefore a single-valued function of position. In the Lagrangian description, by contrast, one does not average, and since there are usually several particles in every small volume, the flow velocity of the particle phase can be multi-valued. In particular, when particles go past each other, we have the formation of caustics. This implies that particles of the same size can have opposite velocities at the same location, creating phase-space singularities. In the Eulerian approach, this situation would lead to the formation of shocks – even for dilute particle populations. In

the Lagrangian approach, by contrast, particle populations can go through each other without any interaction.

Caustic formation can be an important pathway to enhanced particle interaction (Wilkinson & Mehlig 2005; Bec *et al.* 2010; Gustavsson *et al.* 2012; Voßkuhle *et al.* 2014). This applies mainly to particles large enough to decouple from the carrier fluid and this phenomenon can be the main reason why such particles interact. At high Mach numbers, it is mainly shock interaction and compression of the carrier fluid when shocks meet that matters. This is because the density increase due to compression is by far the greatest effect.

A more commonly studied route to enhanced interaction rates is the centrifugal effect of turbulent eddies, which fling the particles to the edges of the eddies (Maxey & Riley 1983; Maxey 1987; Squires & Eaton 1991; Eaton & Fessler 1994; Bec 2003; Bec *et al.* 2007; Bhatnagar *et al.* 2018; Yavuz *et al.* 2018). This is because the particles do not experience the confining pressure that keeps the gas on closed streamlines. The relative importance of caustics and the centrifugal effects is not well understood (Voßkuhle *et al.* 2014). One of the goals of the present study is therefore to assess their roles separately for vortical and acoustic turbulence. This assessment will be based on the knowledge that caustics are only captured by the Lagrangian approach while the centrifugal effect is captured both by the Lagrangian and the Eulerian approaches.

The Lagrangian and Eulerian descriptions are complementary and can also be used to gauge their respective regimes of validity. This allows us to study, for example, when and at what length scales statistical noise becomes important, and when caustics formation becomes important. We focus on three-dimensional simulations, but we also use one-dimensional simulations, where caustic formation can be studied in isolation.

In both types of approaches, we ignore the back-reaction of particles on the flow. This can become important at large mass loading parameters and can lead to other interesting effects such as the streaming instability (Johansen & Youdin 2007) and the resonant drag instability (Squire & Hopkins 2017), which will not be addressed here. We also neglect gravity and tidal forces.

2. The model

We consider an isothermal gas where the pressure is proportional to the density ρ and is given by $\rho c_{\rm s}^2$, with $c_{\rm s}$ being the isothermal sound speed. The velocity of the gas $\boldsymbol{u}$ is governed by the Navier-Stokes and continuity equations,

$$\frac{\partial \boldsymbol{u}}{\partial t} + \boldsymbol{u}\cdot\boldsymbol{\nabla}\boldsymbol{u} = -c_{\rm s}^2\boldsymbol{\nabla}\ln\rho + \boldsymbol{f} + \rho^{-1}\boldsymbol{\nabla}\cdot(2\rho\nu\mathsf{S} + \rho\zeta_{\rm shock}\mathsf{I}\boldsymbol{\nabla}\cdot\boldsymbol{u}), \tag{2.1}$$

$$\frac{\partial \ln\rho}{\partial t} + \boldsymbol{u}\cdot\boldsymbol{\nabla}\ln\rho = -\boldsymbol{\nabla}\cdot\boldsymbol{u}, \tag{2.2}$$

where $\boldsymbol{f}$ is a stochastic forcing term, ν is the kinematic viscosity, I is the unit matrix with indices $\mathsf{I}_{ij}=\delta_{ij}$, and S is the trace-less rate of strain tensor with the components

$$\mathsf{S}_{ij} = \tfrac{1}{2}(\partial u_i/\partial x_j + \partial u_j/\partial x_i) - \tfrac{1}{3}\delta_{ij}\boldsymbol{\nabla}\cdot\boldsymbol{u}. \tag{2.3}$$

The forcing term consists either of random plane waves (vortical forcing) that are δ-correlated in time (see Haugen *et al.* 2012, for details), or of localised pressure enhancements (compressive forcing) with $\boldsymbol{f}=-\boldsymbol{\nabla}\phi$, where ϕ is a Gaussian in space at new locations in regular time intervals $\delta t_{\rm f}$ (Mee & Brandenburg 2006). The amplitude of the forcing is denoted by f_0.

In most of the simulations presented here, we perform direct numerical simulations

(DNS). In those cases, $\zeta_{\rm shock}=0$. However, to save resources, especially in astrophysics, one often uses a shock-capturing viscosity (von Neumann & Richtmyer 1950). This broadens the shocks and allows one to resolve them on a coarser mesh. To assess the effect of such an artificial treatment on the particle clustering, in some cases we compare the results from the DNS with runs where a coarser mesh is used together with a shock-capturing viscosity. We adopt the shock capturing viscosity of von Neumann & Richtmyer (1950), which corresponds to a bulk viscosity with

$$\zeta_{\rm shock}=C_{\rm shock}\delta x^2\langle-\boldsymbol{\nabla}\cdot\boldsymbol{u}\rangle_+. \tag{2.4}$$

Here, $\langle ...\rangle_+$ denotes a running five point average over all positive arguments, corresponding to a compression; see Caunt & Korpi (2001) and Haugen *et al.* (2004) for a detailed description. In contrast to the DNS, we refer to those simulations as large eddy simulations (LES).

In both the Lagrangian and Eulerian descriptions, the velocity $\boldsymbol{v}_p$ of the particle with index p couples to the gas through the friction force,

$$\boldsymbol{F}_p=-\frac{1}{\tau_p}\left(\boldsymbol{v}_p-\boldsymbol{u}\right). \tag{2.5}$$

For the flows considered here, the particle response time is given by a term that is slightly different for dense and dilute gases. When the mean-free path of the gas molecules is short, the response time is given by the Stokes time, modified by a Reynolds number-dependent factor of the form

$$\tau_p^{\rm St}=\frac{2}{9}\frac{\rho_p}{\rho}\frac{a_p^2}{\nu}\left(1+0.15\,Re_p^{0.687}\right)^{-1}, \tag{2.6}$$

where a_p and ρ_p are the radius and material density, respectively, and ${\rm Re}_p=a_p u_{\rm rms}/\nu$ is the particle Reynolds number. For rarefied gases, the response time is based on the Epstein drag and is given by (Schaaf 1963; Kwok 1975; Draine & Salpeter 1979; Mattsson *et al.* 2019*b*)

$$\tau_p^{\rm Ep}=\sqrt{\frac{\pi}{8}}\frac{\rho_p}{\rho}\frac{a_p}{c_{\rm s}}\left(1+\frac{9\pi}{128}\frac{\left|\boldsymbol{u}-\boldsymbol{v}_p\right|^2}{c_{\rm s}^2}\right)^{-1/2}. \tag{2.7}$$

The second term inside of the parenthesis becomes important at large Mach numbers. In the following, we assume that the physical size of particles is always smaller than the Kolmogorov size of the turbulence.

In the Lagrangian description, the evolution of a particle p with velocity $\boldsymbol{v}_p$ at position $\boldsymbol{x}_p$ is given by

$$\frac{d\boldsymbol{v}_p}{dt}=\boldsymbol{F}_p,\quad \frac{d\boldsymbol{x}_p}{dt}=\boldsymbol{v}_p, \tag{2.8}$$

where we have ignored the effects of Brownian motion, which leads to the diffusion of particles. In the associated Eulerian description, diffusion is included and, instead of equation (2.8), we solve instead

$$\frac{\partial\boldsymbol{v}_p}{\partial t}+\boldsymbol{v}_p\cdot\boldsymbol{\nabla}\boldsymbol{v}_p=\boldsymbol{F}_p+\frac{2}{\rho_p}\boldsymbol{\nabla}\cdot(\rho_p\nu_p\mathsf{S}_p), \tag{2.9}$$

$$\frac{\partial n_p}{\partial t}+\boldsymbol{v}_p\cdot\boldsymbol{\nabla}n_p=-n_p\boldsymbol{\nabla}\cdot\boldsymbol{v}_p+\kappa_p\nabla^2 n_p, \tag{2.10}$$

where n_p is the particle number density and ν_p and κ_p are artificial viscosity and diffusivity for the particle fluid (denoted now by p collectively for all particles). Those terms are needed for reasons of numerical stability.

We use medium-resolution ($N_{\rm mesh}^3 = 256^3$ and 512^3) in three-dimensional (3D) triply periodic cubic domains with side lengths L and the number of mesh points in each direction being $N_{\rm mesh}$. The smallest wavenumber in the domain is then $k_1 = 2\pi/L$. Unless otherwise specified, dust particles are included as inertial particles in 5 size bins with 4×10^6 particles in each (for the Lagrangian simulations). We use the PENCIL CODE (Pencil Code Collaboration *et al.* 2021), which is a high-order, finite-difference code (sixth order in space and third order in time); see also Brandenburg & Dobler (2002) for details.

In some of the tables in this paper, we also give the dimensional values of f_0, $\delta t_{\rm f}$, ν, etc. Those are based on our choice $c_{\rm s} = 2k_1 = \langle\rho\rangle = 1$ in the numerical calculations. In all cases, we use $\rho_p = 10^3$.

3. Diagnostic tools

3.1. *Non-dimensional numbers*

The flow is characterised by the Reynolds and Mach numbers,

$$Re = \frac{u_{\rm rms}}{\nu k_{\rm f}} \quad \text{and} \quad Ma = \frac{u_{\rm rms}}{c_{\rm s}}, \tag{3.1}$$

respectively, where $k_{\rm f}$ is the forcing wavenumber. The behaviour of the particles is characterised by the Stokes numbers

$$St_{\rm int} = \tau_p/\tau_{\rm f} \quad \text{and} \quad St_{\rm Kol} = \tau_p/\tau_{\rm Kol}, \tag{3.2}$$

where τ_p is the particle response time, $\tau_{\rm f} = k_{\rm f}/u_{\rm rms}$ is the time scale related to the size of large-scale fluid structures, e.g., the forcing scale, and $\tau_{\rm Kol} = \sqrt{\nu/\epsilon_{\rm K}}$ is the Kolmogorov time, where $\epsilon_{\rm K} = \langle 2\rho\nu\mathbf{S}^2\rangle$ is the energy dissipation rate. Both variants of the Stokes number are related to particle clustering due to particle inertia. For small Mach numbers, ρ is close to the mean density $\overline{\rho}$, allowing us to express $\epsilon_{\rm K}$ also in terms of the energy spectrum $E(k)$. They are normalised such that $\int E(k)\,{\rm d}k = \overline{\rho}\langle\boldsymbol{u}^2\rangle/2$. We then have $\epsilon_{\rm K} = 2\overline{\rho}\nu\int k^2E(k)\,{\rm d}k$. Also of interest is the associated Kolmogorov scale $\ell_{\rm Kol} = (\nu^3/\epsilon_{\rm K})^{1/4}$.

The Knudsen number of particles of a certain size is defined as the ratio of the mean free path λ of the gas molecules to the size of the particle, i.e., $Kn = \lambda/d_{\rm p}$. The drag force on the particles is inversely proportional to the particle response time; see Eq. (2.5). For a continuous fluid, where the Knudsen number is much smaller than unity, the particle response time is given by the Stokesian time; see Eq. (2.6). For rarefied gases, however, the mean free path is large compared to the particle size and the response time is then given by the Epstein time, as given in Eq. (2.7).

The dimensionless particle size parameter (see Hopkins & Lee 2016) is defined as

$$\alpha = \frac{\rho_p}{\langle\rho\rangle}\frac{a_p}{L_{\rm f}}, \tag{3.3}$$

where $L_{\rm f}$ is taken to be the physical forcing scale of the turbulent flow. For small values of Kn, we find that the mean Stokes number is

$$\langle St_{\rm int}\rangle = \frac{\langle\tau_p^{\rm St}\rangle}{\tau_{\rm f}} \approx \frac{(2/9)\,\alpha\,Re_p}{1+0.15\,Re_p^{0.687}} \sim \alpha\,Re_p, \tag{3.4}$$

while in the Epstein limit we find

$$\langle St_{\rm int}\rangle = \frac{\langle\tau_p^{\rm Ep}\rangle}{\tau_{\rm f}} \approx \sqrt{\frac{\pi}{8}}\,\alpha\,\mathcal{M}_{\rm rms}\left(1+\frac{9\pi}{128}\frac{|\boldsymbol{u}-\boldsymbol{v}_p|^2}{c_{\rm s}^2}\right)^{-1/2} \sim \alpha\,\mathcal{M}_{\rm rms}. \tag{3.5}$$

From these two relations one can see that, while $St_{\rm int}$ for a given particle size in the Epstein limit is mainly affected by compression and essentially unaffected by viscosity of the carrier fluid, it is inversely proportional to the viscosity in the Stokes limit.

3.2. *Power spectra of particle density*

To measure preferential clustering at all scales, from the smallest scale resolved in the simulation to the size of the simulation box, we compute power spectra of n_p as (Haugen *et al.* 2018)

$$P_n(k) = \frac{1}{2} \sum_{k-\delta k/2 \leqslant |\boldsymbol{k}| < k+\delta k/2} |\hat{n}_p(\boldsymbol{k})|^2 \, \mathrm{d}^3\boldsymbol{k}, \tag{3.6}$$

where $\hat{n}_p(\boldsymbol{k}) = \mathcal{F}\left(n_p(\boldsymbol{x})\right)$ is the Fourier transform of n_p, $\boldsymbol{k} = (k_x, k_y, k_z)$ is the wavevector, and the integration is over concentric shells in wave number space. From the above, we see that

$$\int_{k_1}^{k_{\rm max}} P_n(k) \, \mathrm{d}k = \frac{1}{2}\langle n_p^2 \rangle, \tag{3.7}$$

where $k_{\rm max} = k_1 N_{\rm mesh}/2$ is the Nyquist wavenumber, and angle brackets, $\langle ... \rangle$, represent spatial averaging, which means that $\langle n_p^2 \rangle^{1/2}$ is the root-mean-squared particle number density.

If the particles were randomly distributed, $|\hat{n}_p(\boldsymbol{k})|$ would be on average independent of $k = |\boldsymbol{k}|$. In three dimensions, however, the shell integration introduces an additional k^2 factor, so we expect

$$P_n(k) = Ak^2, \tag{3.8}$$

which can be combined with equation (3.7) to yield

$$\frac{1}{2}\langle n_p^2 \rangle = \int_{k_1}^{k_{\rm max}} Ak^2 \, \mathrm{d}k = \frac{A}{3}(k_{\rm max}^3 - k_1^3) \approx \frac{A}{3} k_{\rm max}^3, \tag{3.9}$$

where we have assumed $k_1 \ll k_{\rm max}$, and A is a constant that we shall be concerned with later in Section 4.2.1. We improve on this description further below, when we analyse concrete examples.

4. Results

In this paper, we are concerned with the differences in particle clustering between vortical and compressive forcings. To convey an impression of this phenomenon, we begin by showing in figure 1 the projected particle number densities of snapshots from DNSs with vortical and compressive forcings for Stokes numbers around unity. Evidently, the visual impressions for the two types of flow are rather different. Even though the typical length scales of the forcings are similar in the two cases, the clustering phenomenon is markedly different. For vortical forcing, the overall contrast between minimum and maximum particle concentrations is much smaller than for compressive forcing. In the vortical case, the particle concentrations take a more filamentary and perhaps sheet-like structure, while in the compressive case, the particle concentrations are more spherical in shape.

4.1. *One-dimensional simulations*

To illustrate the effects specific to compressive clustering, let us consider first a one-dimensional shock model as an illustrative example. Here, we also compare the Lagrangian particle simulations with the ones in the Eulerian description.

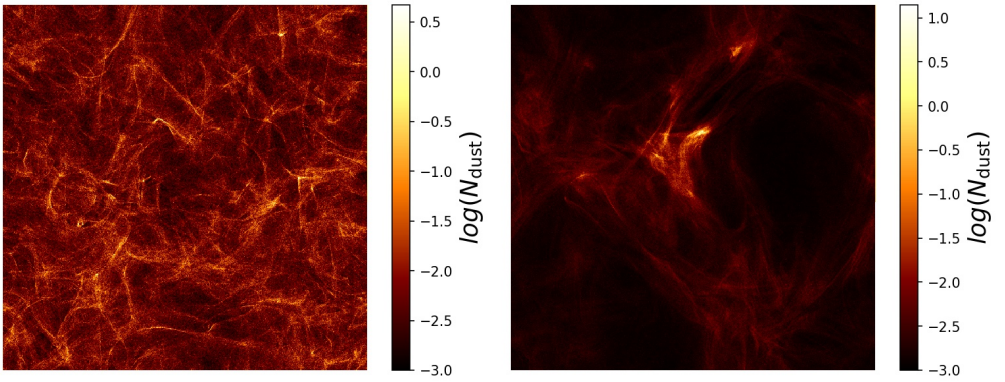

FIGURE 1. Left: Projected particle number density in a snapshot from a DNS with vortical forcing (later referred to as Run V2). Right: the same from a DNS with compressive forcing (later referred to as Run C2). Both cases correspond the particle size showing the most clustering ($St_{\rm int} = 0.31$ and 0.36, respectively).

4.1.1. *Applicability of the Eulerian approach*

Caustics formation in the particle distribution, which is evident from the presence of multi-valued particle velocities, is a phenomenon that cannot be described with the Eulerian approach. For small enough particle inertia, i.e., for small Stokes numbers, the Eulerian and Lagrangian approaches should agree with each other. However, there is also another source of discrepancy. The Lagrangian approach is suitable for modelling dilute systems, but, due to the finite number of particles, it also has the disadvantage of suffering from statistical fluctuations when the intention is to model non-dilute systems, where fluctuations should be small. Statistical noise does not occur in the Eulerian approach. Thus, for dense systems and small Stokes numbers, the Eulerian approach can be beneficial. To determine the limits of applicability of the Eulerian approach quantitatively, we consider a simple one-dimensional model.

We adopt a localised hump in the fluid density, which we model by a Gaussian in $\ln\rho(x)$ at the position $x = 0$ in a domain of size $-\pi/2 < x < 3\pi/2$. Thus, we take

$$\ln\rho[(x)/\rho_0] = \mathcal{A}\exp\left(-x^2/2\sigma_s^2\right), \tag{4.1}$$

where $\mathcal{A}$ is an amplitude factor, ρ_0 is an overall normalisation coefficient, the width is given by $\sigma = 0.35$, and the ratio of the peak value over the background is 3.1. For these simulations we use periodic boundary conditions. The initial density profile launches an acoustic wave; see figure 2 for plots of u_x and ρ at $t = 0.1$ and $t = 0.5$. The front speed exceeds the sound speed when the gas speed approaches a certain fraction of the sound speed; see Appendix for an illustration. We then use the gas velocity and gas density at $t = 0.5$ as initial condition for the particles by setting the particle velocity for all particle sizes equal to the fluid velocity. The particle number density of all particle sizes is set proportional to the gas density.

In figure 3 we show the particle velocities as a function of position for Lagrangian and Eulerian models for particle radii $a_p = 3\times10^{-3}$ and 10^{-1} at different times. We also show the gas velocity, which propagates at a speed slightly faster than the sound speed, $c_{\rm s} = 1$; see Appendix A for a plot showing the numerically obtained dependence of the front speed on the gas speed. The lighter particles follow the fluid and are not shown, but the heavier ones lag behind because they only inherit the speed of the gas at $t = 0.5$, and they are too heavy to get accelerated by the passing acoustic wave. At

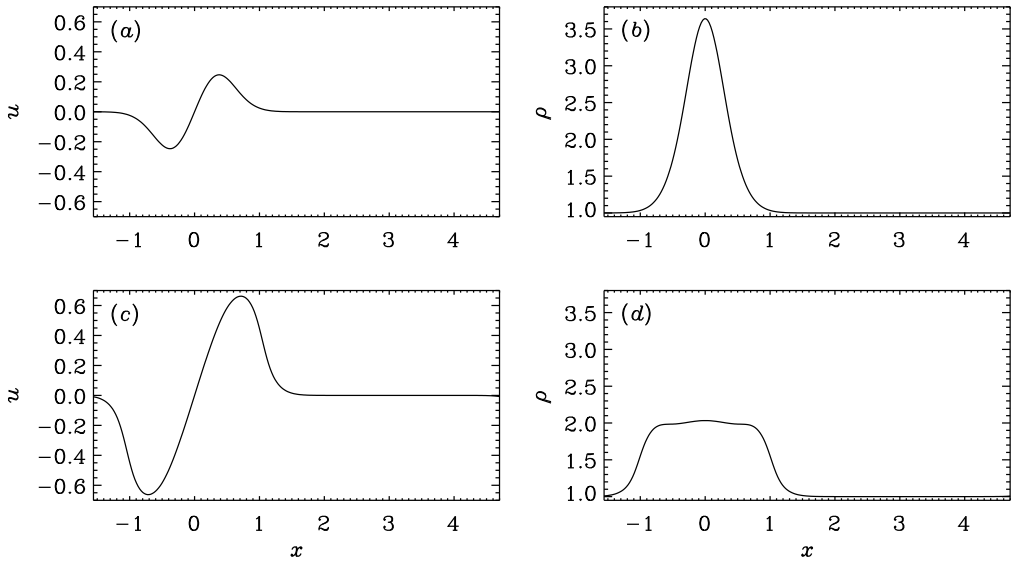

FIGURE 2. (*a*) Gas velocity and (*b*) density at $t = 0.1$ (upper row) and $t = 0.5$ (lower row) in panels (*c*) and (*d*). The data for $t = 0.5$ serve as initial condition for the particles.

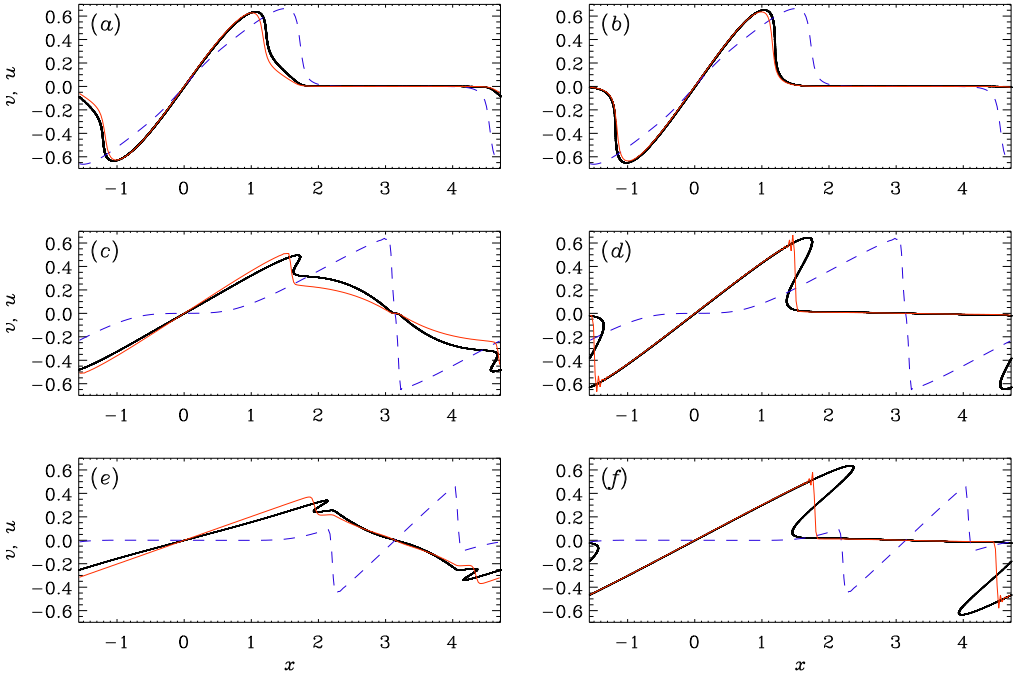

FIGURE 3. Particle velocity in the Lagrangian simulation (black) and the Eulerian one (red), together with the gas velocity (blue) at times $t = 1$, 2, and 3 for $a_p = 3 \times 10^{-3}$ (corresponding to $St_{\rm int} = 1$, panels a, c, and e) and 10^{-1} (corresponding to $St_{\rm int} = 30$, panels b, d, and f).

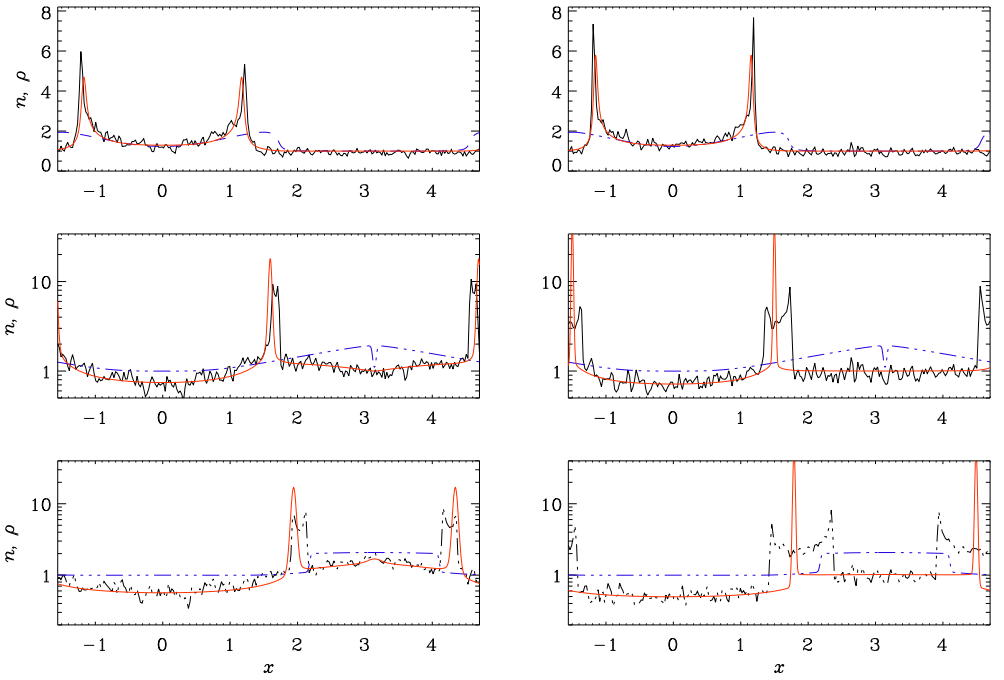

FIGURE 4. Particle density in the Lagrangian simulation (black) and the Eulerian one (red), together with the gas density (blue) at times $t = 1$, 2, and 3. Two particle sizes are shown: $a_p = 3 \times 10^{-3}$ (left column) and 10^{-1} (right column).

early times ($t = 1$), the velocities in the Lagrangian and Eulerian models are close to each other, but at later times the particle velocities in the Lagrangian description become multi-valued, which corresponds to caustics formation. This phenomenon becomes more prominent for the heavier particles since they are not decelerated by the drag from the gas. In the Eulerian description, we instead see the formation of a shock. Away from the shock, the Lagrangian and Eulerian descriptions agree with each other rather well, especially for the heavier particles. To resolve the shock in the Eulerian simulations, we must apply a certain amount of artificial viscosity and diffusivity for the particle fluid. If this artificial viscosity is too small, wiggles occur in the downstream part of the shock, as can already be seen from the profile of $v_x(x)$ in figure 3. Including such artificial viscosity and diffusivity is a purely numerical device to stabilise the solution, but it is likely to introduce errors in the results. By comparing with the Lagrangian approach, we will try to assess the extent of such artifacts.

Snapshots of the particle number densities are shown in figure 4 for the same times and the same two particle sizes as in figure 3. We see the development of extended structures with two enhancements on their flanks, characteristic of caustics, as is correctly reproduced with the Lagrangian approach. The Eulerian approach, on the other hand, yields just a single albeit very strong spike, which may cause an increase of the particle-interaction rate even without any caustics forming.

It is of interest to determine the Stokes number relevant for caustics formation. This is important for knowing the maximum Stokes number for which the Eulerian approximation can still be used. For smaller Stokes numbers, no artificial particle viscosity and diffusivity are needed. For larger Stokes numbers, however, the Eulerian approach can represent the caustics only as shocks, which requires an increasing amount of artificial

Run	p $k_2 a_p$	1 10^{-4}	2 3×10^{-4}	3 10^{-3}	4 3×10^{-3}	5 10^{-2}	6 3×10^{-2}	7 10^{-1}
A	St_p	0.03	0.1	0.3	1.0	3	10	30
B	St_p	0.007	0.02	0.07	0.2	0.7	2.0	6.8

TABLE 1. Stokes numbers for Runs A (Section 4.1.1) and B (Section 4.1.2).

viscosity and diffusivity to keep them numerically resolved. The Stokes number is defined through equation (3.2). For the solution shown in figure 3, we find that the fluid travel time across the width of the front Δx is

$$\tau_{\rm f} = \Delta x/\Delta u \tag{4.2}$$

where Δu is the fluid velocity at the front. For the current experiments, Δx is taken to be the thickness of the front at the time when the particles were introduced in the simulation; see Run A in table 1 for more details about the particles.

In the example discussed above, we have $\tau_{\rm f} = 0.72/0.66 \approx 1.1$, and we find caustics for $a_p \geqslant 10^{-3}$, which corresponds to $p = 3$. To compute the critical Stokes number $St_{\rm crit}$ above which caustics formation occurs, we need to know the ρ_p/ρ ratio, where we take the fluid density on the upstream side of the front, which is here $\rho \approx 1.8$. We used $\rho_p = 10^3$, so, altogether, we have $St_{\rm crit} = 0.30$. This means that, for simulations where the Stokes number is larger than ~ 0.3, the Eulerian particle approach cannot be used. It is important to realise that we are here talking about the Stokes number based on the largest fluid scale, $St_{\rm int}$, and not the Kolmogorov scale. As we shall see below, at the numerical resolutions accessible in our three-dimensional simulations, the difference between $St_{\rm int}$ and $St_{\rm Kol}$ is not very large.

4.1.2. *A mechanism for irrotational supersonic clustering*

It is conceivable that irrotational supersonic flows can yield new ways of clustering that would not occur in vortical subsonic flows. One idea for such a mechanism is that particles of a suitable mass that move toward each other on two colliding shocks, will be decelerated as the shocks collide, but the particles are too heavy to become re-accelerated as the shocks depart again immediately after the collision. The particles will then be left behind after the shocks move away, forming a cluster. To test this idea, we use an experiment similar to that described in Section 4.1.1, but with a stronger density enhancement.

In Section 4.1.1, we used the gas velocity and density at a certain time to reinitialise the particles by setting the particle velocity for all particle sizes to a value equal to the fluid velocity. The initial width of the density distribution is again 0.35. However, the density enhancement of the gas is now so strong that its distribution is so different from a Gaussian that it can no longer be used for reinitialising the particles in a simple way. We therefore reinitialise the fluid density equal to the density of the lightest particles and then set the density and velocity of the heavier particles to the same as the lightest particles. The ratio of the peak value of the density over its background then turns out to be 22. In this experiment, we only use the Lagrangian approach. See Run B in table 1 for more details about the particles.

The result of this experiment is shown in figure 5, where we plot xt diagrams of ρ and n_p for different particle sizes. For small particles with small Stokes numbers, the particles follow the gas. This can be seen by the similarity between panels (a) and (b). To estimate

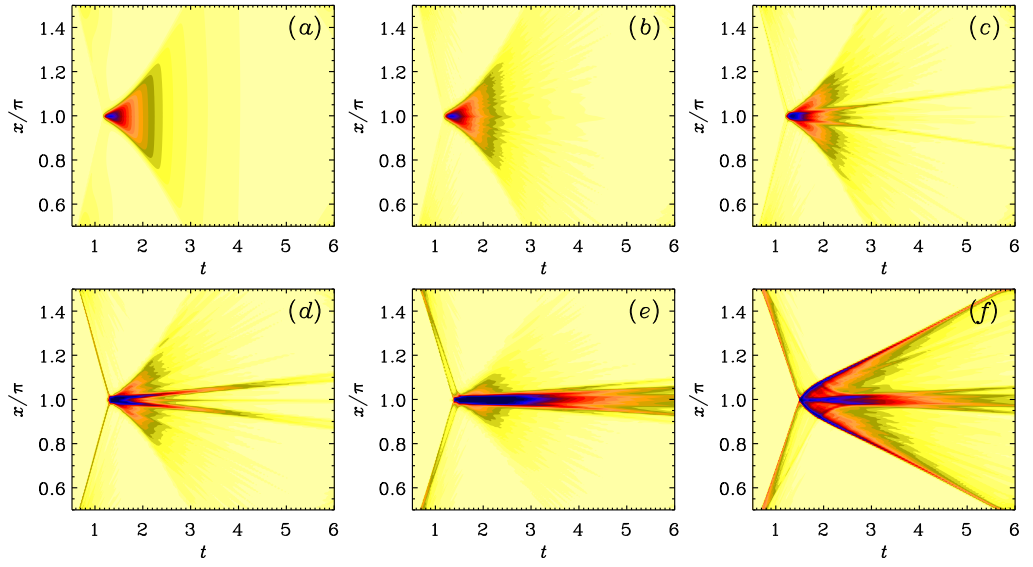

FIGURE 5. xt diagrams of (a) ρ, (b) n_1, (c) n_4, (d) n_5, (e) n_6, and (f) n_7.

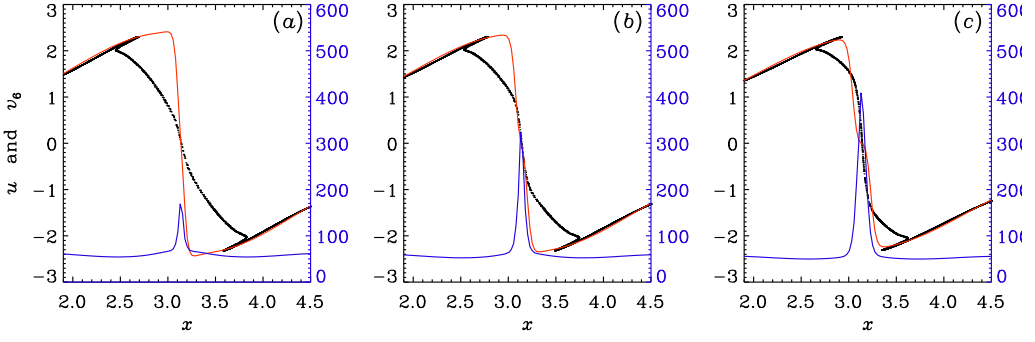

FIGURE 6. Velocity of particles with radius a_6 (black dots) and fluid velocity (red lines), as well as the gas density (blue lines and axes on the right) at $t = 1.18$ (a), close to the time $t_* = 1.16$ when the shocks meet and the gas density develops a peak. Panels (b) and (c) show the same at $t = t_* + \tau_6 = 1.22$ and $t_* + 2\tau_6 = 1.28$.

$St_{\rm int}$ in this case, we used $\Delta u = 2.6$ and $\Delta x = 0.08$, so $\tau_{\rm f} = 0.08/2.6 \approx 0.03$. For our largest particles with $a_p = 0.1$, we find $\rho \approx 300$; see the blue lines in figure 6. We again used $\rho_p = 10^3$, which yields $\rho_p/\rho = 1000/300 \approx 3$. Therefore, $\tau_p = \sqrt{\pi/8}\,(\rho_p/\rho)(a_p/c_{\rm s}) \approx 0.2$, so we have $St_{\rm int} \sim 7$.

For our largest particle size with $St_{\rm int} \approx 7$, the two counter-streaming particle clouds associated with the two opposing shocks tend to run through each other owing to their large inertia, as we can see from figure 5(f). For the intermediate size, where $St_{\rm int} \approx 2$, however, a sizeable particle cloud is left behind at the original position of the collision of the two shocks; see figure 5(e). This critical value is close to unity, as one might have expected. We conclude from this that a particle cluster will form after the collision of two shocks if the Stokes number is around unity. Here, the Stokes number is based on the width and speed of the shock fronts. This mechanism for particle clustering is fundamentally different from the classical eddy mechanism of Maxey & Riley and it

Case	forcing	f_0	$\delta t_{\rm f}$	ν	Ma	Re	$\tau_{\rm kin}$	$\tau_{\rm Kol}$	$St_{\rm int}$	$St_{\rm Kol}$
V1	vort.	0.02	—	0.001	0.15	103	4.3	1.8	7.3×10^{-4}... 7.3	1.7×10^{-3}... 17
V1S	vort.	0.02	—	0.001	0.15	103	4.4	1.8	5.1×10^{-4}... 5.1	1.2×10^{-3}... 12
V2	vort.	0.2	—	0.01	0.67	45	1.0	0.56	3.1×10^{-3}... 31	5.5×10^{-3}... 55
V2a	vort.	0.2	—	0.02	0.59	20	1.13	0.81	2.8×10^{-3}... 28	3.9×10^{-3}... 39
V2b	vort.	0.2	—	0.005	0.71	95	0.94	0.39	3.3×10^{-3}... 33	8.0×10^{-3}... 80
V3	vort.	0.5	—	0.05	1.00	13	0.67	0.50	4.7×10^{-3}... 47	6.3×10^{-3}... 63
V3a	vort.	0.5	—	0.02	1.14	38	0.59	0.32	5.3×10^{-3}... 53	9.9×10^{-3}... 99
C1	comp.	0.5	0.5	0.005	0.19	25	3.53	1.89	8.9×10^{-4}... 8.9	1.7×10^{-3}... 17
C1a	comp.	0.5	0.5	0.002	0.19	64	3.47	1.22	9.0×10^{-4}... 9.0	2.6×10^{-3}... 26
C1.5	comp.	1.5	1.0	0.015	0.39	17	1.72	1.16	2.4×10^{-2}... 54	3.6×10^{-2}... 80
C2	comp.	4.0	1.0	0.02	0.76	25	0.88	0.57	3.6×10^{-3}... 36	5.5×10^{-3}... 55

TABLE 2. Summary of our simulations; "comp" and "vort" refer to compressive and vortical forcings, respectively.

operates only for large enough Mach numbers. For such flows, however, it may be the dominating mechanism.

The biggest uncertainty in our estimate of $St_{\rm int}$ lies in the value of ρ. In the following, we focus on the particles in bin 6, and denote the corresponding velocity by v_6 and the response time of those particles by τ_6. To determine the relevant value of ρ, we show in figure 6 the profiles of $\rho(x)$ together with those of $v_6(x)$ and $u(x)$ at times $t_* + \tau_6/3$, $t_* + \tau_6$, and $t_* + 2\tau_6$, where $t_* = 1.16$ is the time when the shocks meet and the gas density develops a peak. We see that the peak in ρ reaches values of around 400, but at the time $t_* + \tau_6$, the particles will have slowed down considerably. Therefore, the relevant density to be used is the temporally averaged density at the peak until that time, which is below 300.

4.2. *Three-dimensional simulations*

In the previous sections, we studied several aspects of particle clustering in idealised one-dimensional simulations. We will now proceed by turning our attention to fully three-dimensional turbulence simulations. As described in Section 2, two kinds of forcings are employed in this work. In table 2, run names starting with "V" use vortical forcings, while those starting with "C" adopt spherical expansion wave forcing (compressive forcing). The numbers behind those letters indicate different forcing strengths, which yield different Mach numbers. Different Reynolds numbers are indicated by letters a and b. The run with Stokes drag is denoted by the letter S at the end. We also compare with corresponding Eulerian models (table 3), where we have included an artificial viscosity and diffusivity in order to stabilise the simulations; see equations (2.9) and (2.10).

Contour plots of particle number density are shown in figure 7 for Run V2b. It is clearly seen that the clustering is strongest for our intermediate Stokes numbers, $St_{\rm int} = 0.33$ and 3.3; see figures 7(b) and (c). For the very smallest and largest Stokes numbers, we see almost no clustering; see figures 7(a) and (d). In those cases, the values of α are 0.7 and 7, respectively, where we have used $L_{\rm f} = k_{\rm f}^{-1}$.

In figure 8, we show scatter plots of the particle number density as a function of fluid density for all fluid grid cells in the domain. In the left panel, showing results for the

Case	forcing	f_0	$\delta t_{\rm f}$	ν	ν_p	Ma	Re	$N_{\rm mesh}$
V1	vort.	0.02	—	0.001	0.005	0.15	103	256
V2	vort.	0.2	—	0.01	0.01	0.67	45	512
C1	exp.	0.5	0.05	0.002	0.001	0.19	96	512
C2	exp.	4.0	1.0	0.05	0.05	0.72	14	512

TABLE 3. Summary of Eulerian runs. For all these runs, the artificial diffusivity (κ_p) equals the artificial viscosity (ν_p).

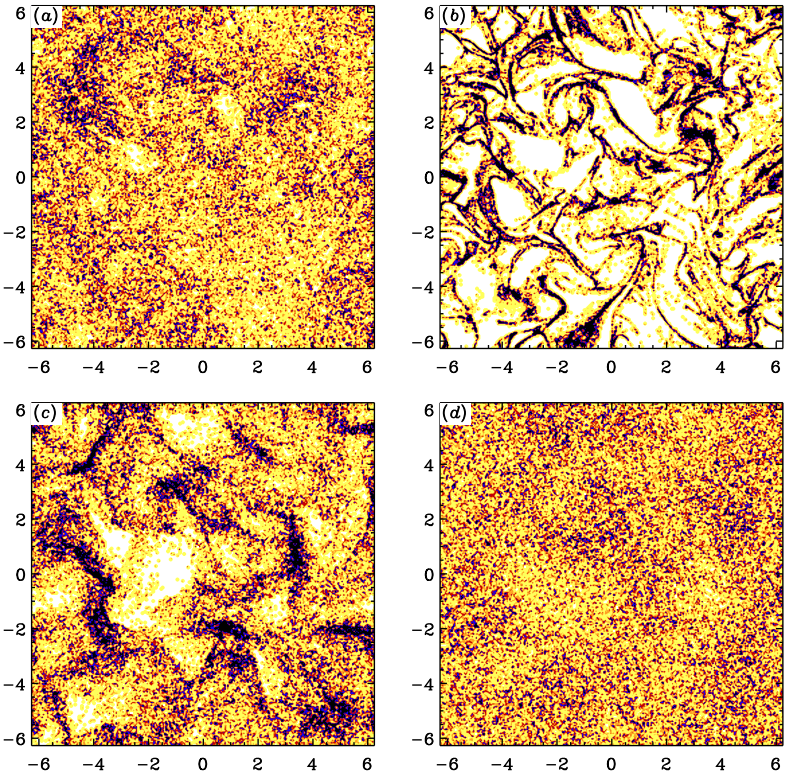

FIGURE 7. Contour plots of particle number density for (a) $St_{\rm int} = 0.033$, (b) 0.33, (c) 3.3, and (d) 33 for case V2b. The particle number density has been integrated over the perpendicular direction for four mesh zones.

smallest Stokes numbers, we see that there is a strong correlation between the two. This is because these small particles follow the fluid almost perfectly, which means that, when the fluid is compressed (high fluid density), the particle field is also compressed (high particle number density). When the Stokes number is increased, but is still rather small, we see in figure 8(b) that the two fields are only weakly correlated. Finally, for those Stokes numbers where we see the strongest clustering in figure 7(b), we show in figure 8(c) that there is no correlation between particle and fluid densities. We can also see the effect of the inertial clustering itself in that there is a large number of grid cells without any

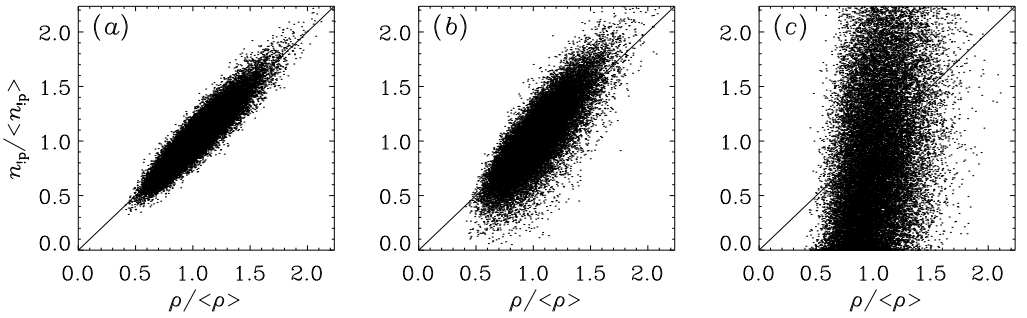

FIGURE 8. Scatter plot of particle number density as a function of fluid density for the three smallest particle sizes of case V2b.

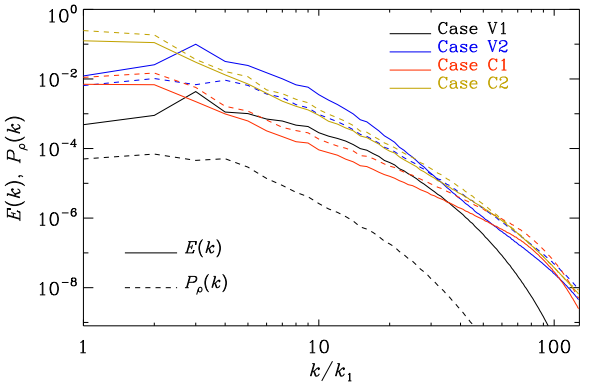

FIGURE 9. $E(k)$ (solid lines) and $P_\rho(k)$ (dashed lines) for our main cases (V1, V2, C1, and C2).

particles ($n_p = 0$), while there is also a significant number of grid cells containing many particles ($n_p > 2$), which is not the case for the smaller Stokes numbers.

4.2.1. *Kinetic energy and density power spectra*

In this paper, we make extensive use of particle power spectra. In this context, it is useful to show first the relevant spectra for the gas. In figure 9, we show kinetic energy spectra together with power spectra of the gas density for cases V1, V2, C1, and C2. The peak of the kinetic energy spectrum occurs at $k/k_1 = 3$ for the cases with vortical forcings (V1 and V2). This wavenumber indicates where the main power of the external forcing is found. For the cases with compressive forcing, however, the peak in the kinetic energy spectrum is found for k/k_1 between 1 and 2. The density power spectra follow the kinetic energy spectra fairly well, although there is a vertical shift. For the compressive forcing, we are driving strong flow divergencies, which results in $P_\rho(k)$ being large compared to $E_{\rm K}(k)$. Since the vortical forcing is divergence-free, the corresponding density variation is small, as seen through the smaller values of $P_\rho(k)$ compared to $E_{\rm K}(k)$. We can also see that the extent of the vertical shift is larger for smaller Mach numbers. This is because the fluid is less compressed for smaller Mach numbers.

4.2.2. *Initial and tracer particle spectra*

In the following, we study power spectra of particle number densities for particles that are embedded in a fluid where turbulence is generated either with vortical or compressive forcing (Runs V1–V3 and Runs C1–C2, respectively). Since particles are tracked in a

Lagrangian fashion, it is convenient to allocate each Lagrangian particle to the nearest Eulerian neighbours in each direction in the fluid mesh. In this way, for every particle size, we generate a variable on the fluid mesh that contains the number of particles that reside within or in the neighbourhood of a given grid cell. These variables can now be used to calculate the particle power spectra for each particle size. The size of the neighbourhood of grid cells that will be influenced by a given particle depends on the interpolation scheme used, which in our case is a second order linear scheme (Johansen *et al.* 2007).

Initially, the particles are randomly distributed over the entire simulation box. This means that the initial power spectra for the different particle sizes are just white noise, which corresponds to a k^2 spectrum; see Section 3.2. If every particle is associated solely with the very nearest grid point of the Eulerian mesh, the k^2 scaling would then be valid for the full wavenumber range. For the current work, however, the contribution from a particle is distributed over several nearby grid points through a linear interpolation scheme. This means that the k^2 scaling will not extend all the way to the largest wavenumbers. Instead, for $k > k_*$, the spectrum, hereafter $P_{n,\mathrm{noise}}$, becomes less steep and eventually reaches a maximum, before it goes down towards the very end.

In analogy with equation (3.9), we now get

$$\frac{1}{2}\langle n_p^2\rangle = \int_{k_1}^{k_{\max}} P_{n,\mathrm{noise}}(k)\,\mathrm{d}k = \int_{k_1}^{k_{\max}} A\tilde{k}^2\,\mathrm{d}k \equiv \frac{A}{3}\tilde{k}_{\mathrm{eff}}^3, \tag{4.3}$$

where $\tilde{k} = k/[1+(k/k_*)^3]$ has been substituted for k in order to account for the departure from k for $k \gtrsim k_* \equiv \kappa k_{\max}$, with $\kappa \approx 0.789$ being a parameter proportional to the position of the local maximum of $P_n(k)$. This implies that $P_{n,\mathrm{noise}} = A\tilde{k}^2$. Defining therefore $\kappa = k_*/k_{\max}$, we find $\tilde{k}_{\mathrm{eff}}^3 = (1+\kappa)(1-\kappa+\kappa^2)/\kappa^3 k_{\max}^3 \approx (1.45\,k_{\max})^3$. By re-arranging the above equation, the constant A, defined in Section 3.2, is found to be $A = 3(\langle n_p^2\rangle/2)/\tilde{k}_{\mathrm{eff}}^3 \approx 0.49\langle n_p^2\rangle/k_{\max}^3$. Together with equation (3.8) we then obtain the initial power spectrum of the particles as

$$P_{n,\mathrm{noise}} \approx 0.49\,\frac{\langle n_p^2\rangle B^2}{k_{\max}^3}\tilde{k}^2, \tag{4.4}$$

where the constant on the right-hand side is defined as $B = \langle\rho\rangle/\langle n_p\rangle$ and is introduced to compensate for the fact that the fluid and particle density fields do not have the same mean value. This compensation is required in order to obtain equation (4.5).

Particles that are very small, having essentially vanishing Stokes numbers, will follow the gas perfectly. If the fluid is incompressible, particles will be re-shuffled owing to turbulence, but their mean separation will be unchanged with time, which means that there is no particle clustering. Hence, the power spectrum of tracer particles in an incompressible fluid would equal $P_{n,\mathrm{noise}}$ for all times. If, however, the fluid is compressible, the compression of the fluid may be so strong that the resulting fluctuations in particle number density becomes larger than the white noise. The particle power spectrum will then be the same as the one for the fluid density. For tracer particles we therefore expect the power spectrum of the particles to be given by

$$P_{n,\mathrm{model}}(k) = P_\rho(k) + P_{n,\mathrm{noise}}(k). \tag{4.5}$$

In figure 10(*a*), we compare the calculated particle spectra from the simulations $P_n(k)$ (solid lines) with the modelled spectra $P_{n,\mathrm{model}}(k)$ (dashed lines) for the four runs V1, V2, C1, and C2 for the lightest particles. We see that the calculated and modelled spectra are remarkably similar for all cases. The k^2 part of the spectrum is a real physical effect

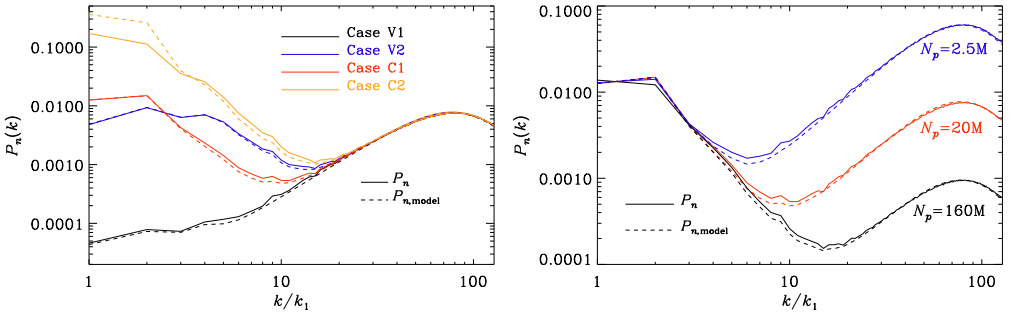

FIGURE 10. Left: Power spectra of particle number density for the smallest Stokes numbers, which are essentially tracer particles (solid lines) for cases V1, V2, C1, and C2. The dashed lines denote the model spectrum as presented in equation (4.5). Right: Comparison of numerical power spectra (solid) and model spectra using equation (4.5) (dashed) for the smallest particles of Run C1 with $N_p = 2.5 \times 10^6$ (blue), 20×10^6 (red), and 160×10^6 (black).

and is a result of having a finite number of particles in the simulation, such a feature cannot be seen if the particles are tracked by the Eulerian approach. Instead, one would then see that the particle spectra follow the fluid density spectrum for all wavenumbers. Unless the particle suspension consists of an infinite number of particles, this behaviour is incorrect and is due to the fact that the Eulerian approach treats the particle suspension as a continuous fluid and not as a collection of a finite number of discrete particles.

In figure 10(b), we show the numerical particle spectra for the particles with the smallest Stokes number of Run C1, obtained with three different numbers of particles (solid lines). The numerical results are then compared with the model data given by equation (4.5). We see that the model results reproduce the simulation results for all particle numbers. But, more importantly, we note that the effect of the finite number of particles becomes less dominant when the number of particles is increased, which is as expected. For the black line ($N_p = 160 \times 10^6$), 10 times more particles than fluid mesh points were used. This highlights the difficulty in exploring weak clustering at large wavenumbers for large Reynolds numbers.

4.2.3. *Comparison of cases with Epstein and Stokesian drag*

For rarefied gases, the molecular mean free path is large compared to the particle size, and the response time is then given by the Epstein time, as presented in Eq. (2.7). For a dense (continuous) fluid, however, where $Kn < 1$, the response time is given by the modified Stokes time; see Eq. (2.6). To compare the effect of using these two response times, we show in figure 11 power spectra of particle number densities for simulations using Epstein and Stokes drags for approximate Stokes numbers between 6×10^{-4} and 6. We see that the two reflect rather similar trends. At least part of the remaining discrepancies can probably be explained by small differences in the actual Stokes numbers for the two drag laws. Both for small and large Stokes numbers, we see a k^2 spectrum, indicative of random particle distributions at high wavenumbers (small scales). Initially, particles of all sizes were randomly distributed, and hence they had a k^2 spectrum. However, the reason that we still see a k^2 spectrum at later times are different for the smallest and largest particles. The largest particles are so heavy that their response times are far too long for the particles to be able to react to the turbulent eddies associated with the smallest spatial and temporal scales. This is why the power spectra of the heavier particles still show their initial k^2 spectrum at small scales. The smallest particles, by contrast, are being re-shuffled by the turbulence and therefore

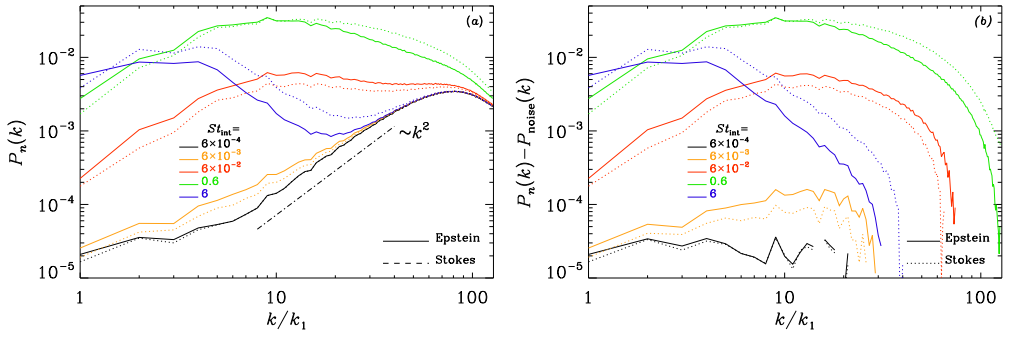

FIGURE 11. Comparison of power spectra of particle number densities for Run V1 using Epstein (solid lines) and Stokes drag (dashed lines) for $St_{\rm int} = 6 \times 10^{-4}$ (black), 6×10^{-3} (red), 6×10^{-2} (orange), 0.6 (green), and 6 (blue) for (a) $P_n(k)$ and (b) $P_n(k) - P_{\rm noise}$.

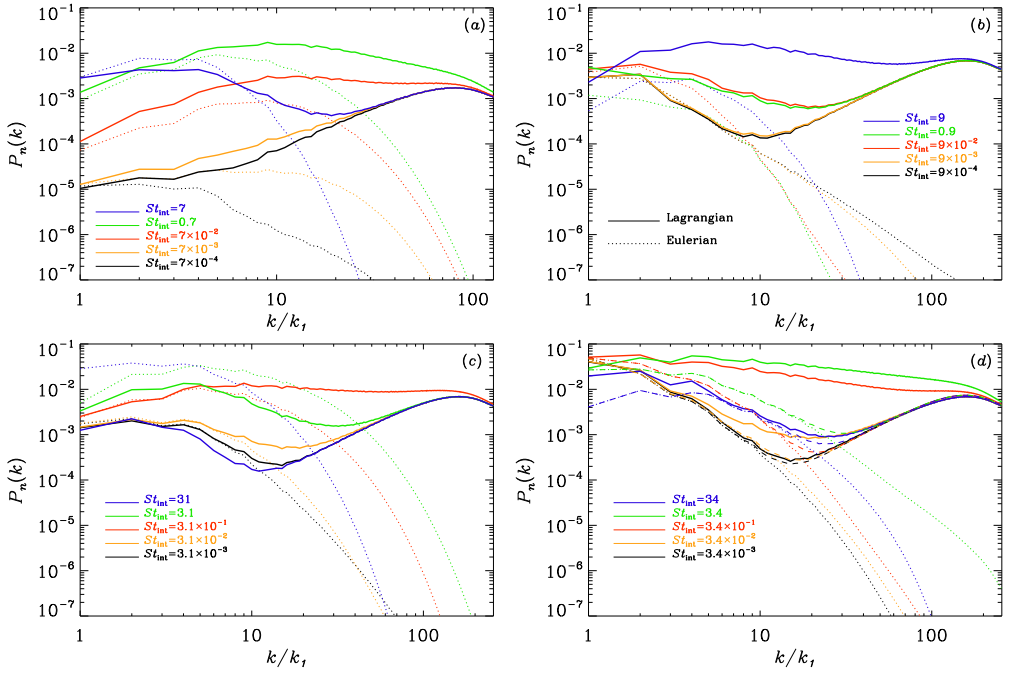

FIGURE 12. Comparison of power spectra of particle number densities for Runs V1 (*a*), C1 (*b*), V2 (*c*), and C2 (*d*).

maintain a random particle distribution. They do not have enough inertia to move from one fluid element to another, which is a requirement for the particles to form inertia-based clusters. They are fundamentally different from the short-lived increase in the particle number density, which occurs always when the fluid volume in which the tracer particles reside, is compressed – for example due to the passing of an acoustic wave or shock.

4.2.4. *Applicability of the Eulerian approach for particles*

In figure 12, particle power spectra for different Stokes numbers are shown for our four main runs, V1, V2, C1, and C2. The solid lines correspond to results obtained with the Lagrangian approach for the particles, while the Eulerian particle approach was used for the simulations visualised by the dotted lines. For V1 and V2, as shown in figure 12(*a*)

and (*c*), we see that the two approaches yield similar results for the smaller Stokes number up to the wavenumbers where the k^2 scaling commences in the Lagrangian simulations, which corresponds to $k \sim 4k_1$ for the 5×4 million particles chosen for these simulations with five different radii. When the Stokes number is increased (different colours), the Lagrangian and Eulerian spectra for $k/k_1 \leqslant 4$ are still comparable for V1, but for V2 we see a clear difference for the largest Stokes numbers, and not just for the largest wavenumbers.

We recall that in the 1-D simulations, the critical value of St_{int} for the occurrence of caustics was around 0.3; see the discussion at the end of Section 4.2.4. In the present case of 3-D turbulence, we also see a difference between the Eulerian and Lagrangian simulations near $St_{\text{int}} = 0.3$, but only for the spherical expansion waves; see figure 12(d). When the turbulence is driven compressively, as in Runs C1 and C2, which are shown in figures 12(b) and (d), we see that the Eulerian and Lagrangian approaches yield comparable results only for the very smallest Stokes numbers. Thus, the range of applicability of the Eulerian approach depends on the type of forcing and is more restrictive in the compressive case. For the other cases, the differences are rather small, except perhaps for the heaviest particles. This difference could also be caused by our usage of artificial viscosity and diffusivity in the Eulerian simulations. At large wavenumbers, on the other hand, there is always a large difference, but this is mainly caused by the effect of noise.

For Run C2 in figure 12(d), we also show the power spectra from the Eulerian approach with the contribution from $P_{n,\text{noise}}$ of equation (4.4) being added. This models a power spectrum that is accounting for the noise from a finite number of Lagrangian particles; see the dashed lines. For the smallest Stokes number, we see that the solid and dashed lines almost overlap, but for all other Stokes numbers the resemblance is poor. This means that, except for the very smallest Stokes numbers, the differences between the particle power spectra obtained with the Lagrangian and Eulerian particle approaches are *not* primarily due to the noise contribution of the Lagrangian approach. Furthermore, from the results shown in figure 12, we can also conclude that the Eulerian approach should *not* be used to track particles unless the Stokes number is low.

As expected from the discussion above (Section 4.2.2), we notice a k^2 behaviour for the smallest Stokes numbers; see figure 12. This applies, of course, only to the Lagrangian simulations with a finite number of particles, and cannot be seen in the corresponding Eulerian simulations. However, there is a clear departure from the k^2 behaviour as the Stokes number is increased. The reason is that particle inertia now starts to have an effect on the clustering. This clustering is not due to fluid compression, but rather due to other inertia-based clustering mechanisms, such as the Maxey–Riley mechanism.

For intermediate Stokes numbers, the particle power spectra resemble those presented in Haugen *et al.* (2018). In that paper, the authors speculate that the peak in the particle power spectra is associated with the similarity in the characteristic time scales of the turbulence and the response time of the particles. However, such a connection could not be confirmed in their work owing to their limited Reynolds number. We see here the same trend as found by Haugen et al., namely that the individual maxima of the spectra are insensitive to the Stokes number. We expect this to change at higher Reynolds numbers and higher resolution.

4.2.5. *Reynolds number dependence*

In order to investigate the nature of the inertia-based clustering further, we would like to run simulations with much larger Reynolds numbers. In the DNS, this becomes very costly when the Mach number is large and shocks need to be resolved. In figure 13,

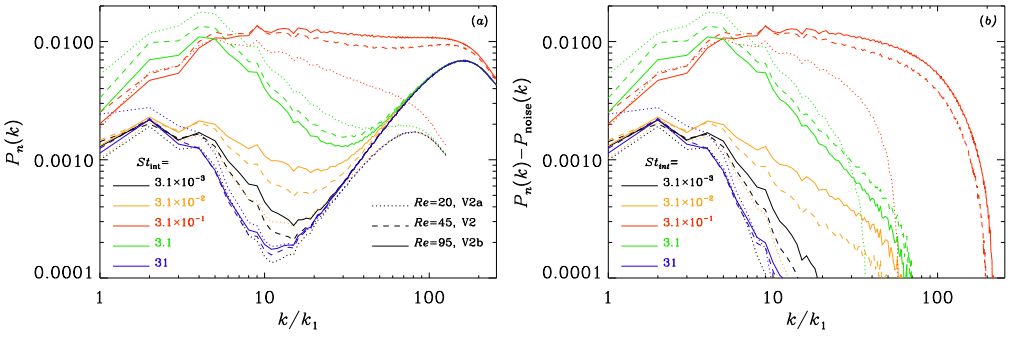

FIGURE 13. Comparison of power spectra of particle number densities for Run V2 (dashed lines) with Run V2a (dotted lines) and Run V2b (solid lines) for (a) $P_n(k)$ and (b) $P_n(k) - P_{\rm noise}(k)$.

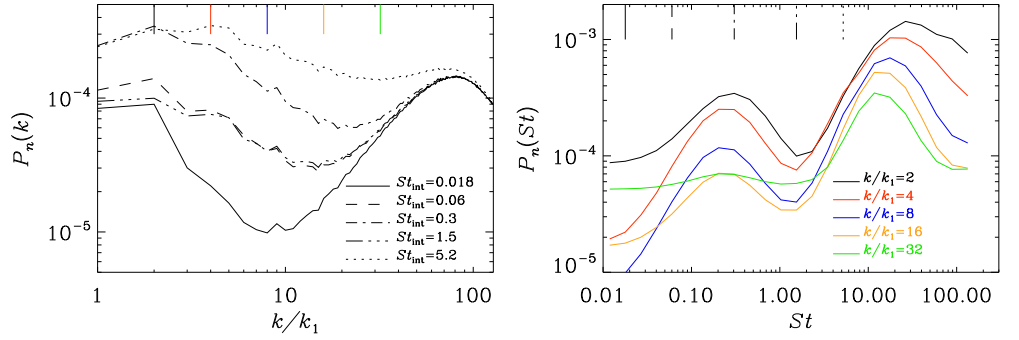

FIGURE 14. $P_n(k)$ and $P_n(St_{\rm int})$ for Run C1 with more particle sizes.

we show the power spectra for different Stokes and Reynolds numbers. For the smaller Stokes numbers, an increase in Re leads to an increase in spectral power. For the larger Stokes numbers, the trend is opposite. Looking at the Kolmogorov-based Stokes number ($St_{\rm Kol}$), however, we see that, for a given value of Re, we get more power and hence more clustering when the Kolmogorov-based Stokes number is closer to unity. For the Reynolds numbers obtained here, it therefore seems that it is the Kolmogorov based Stokes number that controls the strength of the clustering, not the one based on the integral scale ($St_{\rm int}$). The same has also been found in other low Reynolds number studies (Bec *et al.* 2007; Baker *et al.* 2017). As the Reynolds number is increased, however, one eventually reaches a point where particles with $St_{\rm int}$ around unity will be much slower than the smallest turbulent eddies and they will therefore be totally decoupled from the Kolmogorov scale. Hence, the clustering cannot be determined by $St_{\rm Kol}$ in such cases. The nature of this large-scale particle clustering still remains to be understood, because much larger resolution would be needed.

4.2.6. *Clustering mechanisms*

From Run C1, shown in figure 12(b), we see that the spectra for $St_{\rm int} = 0.09$ and 0.9 are very similar. This may be an indication of a non-monotonic behaviour of the spectral evolution with Stokes number. In order to investigate this further, we perform a new simulation that is identical to Run C1 except that we now include many more closely spaced particle sizes (Stokes numbers). The spectra for some of these Stokes numbers are shown in the left-hand panel of figure 14. From this we see that the spectral power increases from $St_{\rm int} = 0.018$ up until $St_{\rm int} = 0.3$, before it decreases again as we

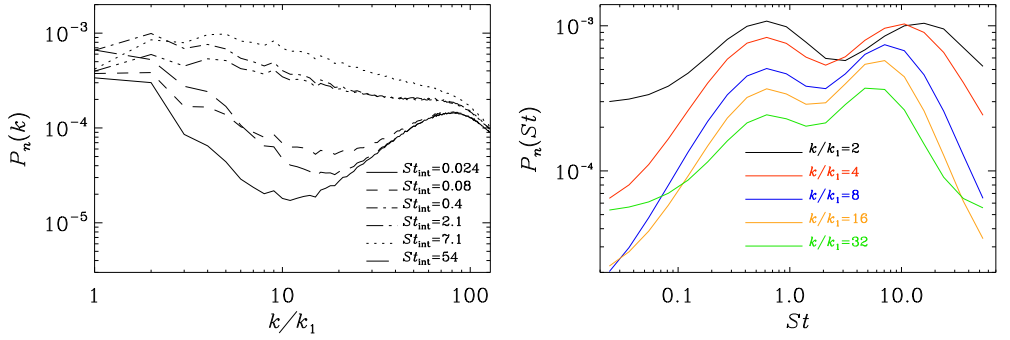

FIGURE 15. Similar to figure 14, but for Run C1.5 with more particle sizes.

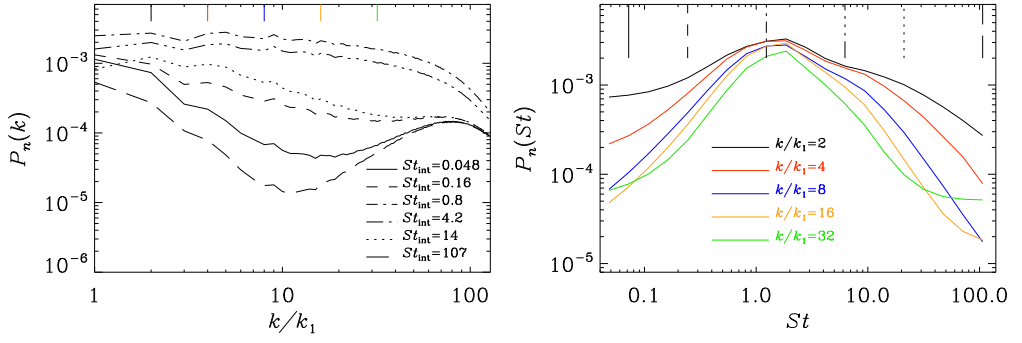

FIGURE 16. Similar to figure 14, but for Run C2 with more particle sizes.

move towards $St_{\text{int}} = 1.5$. Finally, a clear increase is seen for larger Stokes numbers. In the right-hand panel of figure 14 we plot the power for five different wavenumbers as a function of the particle Stokes number in order to see this non-monotonic behaviour more clearly. Here we see that, for all wavenumbers shown, the power spectra attain two distinct maxima: the first is around $St_{\text{int}} = 0.3$, while the other is found between $St_{\text{int}} = 10$ and 30. It is not immediately clear what is causing this non-monotonic behaviour, but we argue here that it is due to a change in the relative importance between two different particle clustering mechanisms. Since compressive forcing was used for this run, the two competing mechanisms are most likely (i) the shock-collision mechanism, as described in Section 4.1.2, and (ii) the classical Maxey–Riley clustering mechanism.

If one of the peaks is due to the shock-collision mechanism, we would expect it to be stronger as the Mach number is increased. We therefore perform an intermediate simulation (Run C1.5) where we increase the Mach number to $Ma = 0.39$ to investigate this. The results are shown in figure 15, where it is clearly seen that the first peak has become substantially stronger, and also moved somewhat to the right. The second peak is, however, almost unchanged, except for a smaller shift to the left. This seems to indicate that it is the first peak that is due to the shock-collision mechanism. We now proceed by increasing the Mach number even further (Run C2) and show the results in figure 16. The first peak has now become so strong that the second peak is only visible as a weak shoulder for $St_{\text{int}} \approx 10$. We will now continue by investigating the mechanism behind the second peak.

For the classical eddy mechanism of Maxey & Riley, we expect the clustering to depend primarily on the vortical part of the velocity field. Hence, the Stokes number for the second peak should be of the order of unity if the fluid time scale is calculated based

Run	$u_{\rm rms}$	$u_{\rm rms}^{\rm vort}$	$u_{\rm rms}^{\rm pot}$	$St_{\rm peak1}$	$St_{\rm peak2}$	$St_{\rm peak1}^{\rm vort}$	$St_{\rm peak2}^{\rm vort}$
C1	0.170	0.017	0.169	0.15	12	0.02	1.2
C1.5	0.352	0.11	0.334	0.6	5	0.19	1.6
C2	0.865	0.200	0.842	2	(7)	0.46	(1.6)

TABLE 4. Rms velocities for the Helmholtz decomposed velocities together with the estimated peak Stokes numbers from the simulations and those based on the vortical velocity field. The numbers in parentheses are more uncertain. The reason for this is that, for Run C2, the second peak appears as a shoulder only, and no clear maximum can be identified.

on the vortical part of the velocity field. To check this, we have performed a Helmholtz decomposition of the velocity field by computing the vector and scalar potential of $\boldsymbol{u} = \boldsymbol{\nabla} \times \psi + \boldsymbol{\nabla}\phi$. The rms values of the corresponding velocity fields are given in table 4. We also list the estimated peak Stokes numbers from the simulations at $k/k_1 = 32$ and those based on the vortical velocity field. We see that the vortical peak Stokes numbers are 1.2 and 1.6 for Runs C1 and C1.5, while for Run C2, we only see an indication of a shoulder at $St_{\rm peak2}^{\rm vort} = 1.6$, at least for smaller values of k. This could be taken as an indication that the second peak is indeed due to the classical eddy mechanism of Maxey & Riley.

In figure 17, we show the particle concentrations for Run C1.5 in order to determine if we can see any trace of the two different mechanisms behind the particle clustering. We see that clustering is now apparent for a very broad range of Stokes numbers, ranging from $St_{\rm int} = 0.3$ to 50. Both for small and large values of $St_{\rm int}$ do we see blob-like clusters, while for intermediate values the structures are more sheet-like. Other than that, there is no real difference in the morphology of structures between small and large Stokes numbers.

In figure 18 we present similar results as in figures 14 and 16, but now for the low Mach-number case with vortical forcing (Run V1). Here there is no indication of anything more than a single peak. This peak, which is due to the classical eddy-clustering of Maxey–Riley, is found to be around $St_{\rm int} \approx 1$, as expected.

4.2.7. *Shock capturing viscosity*

Finally, let us discuss how well the clustering results can be modelled using lower numerical resolution together with a shock viscosity to stabilise the code. To be able to do this, it is interesting to have an even larger value of Ma. Therefore, we consider a DNS with $Ma = 1.14$ (Run V3a) and compare with two LES with different values of $C_{\rm shock}$; see equation (2.4). The result for the density spectra is shown in figure 19. We see that for all values of $St_{\rm int}$, except for $St_{\rm int} = 0.53$, the LES spectra (dashed and dashed-dotted lines) are close to the DNS for $k/k_1 < 20$. For $St_{\rm int} = 0.53$ (red lines), however, the agreement exists only up to $k/k_1 \approx 6$. Surprisingly, a similar departure is not seen in the kinetic energy and fluid density spectra shown in figure 20. A major difference is, of course, that the LES do not resolve the small length scales at all, which is also why their spectra are shorter. The discrepancy in the particle density spectra between LES and DNS therefore suggests that the clustering, which occurs mostly at those intermediate values of $St_{\rm int}$, depends on physical effects at the scale of the shocks, corresponding to high wavenumbers. If this is indeed the case, this departure between DNS and LES may become worse at larger values of Ma. It will be interesting to revisit this question in future simulations at higher resolution.

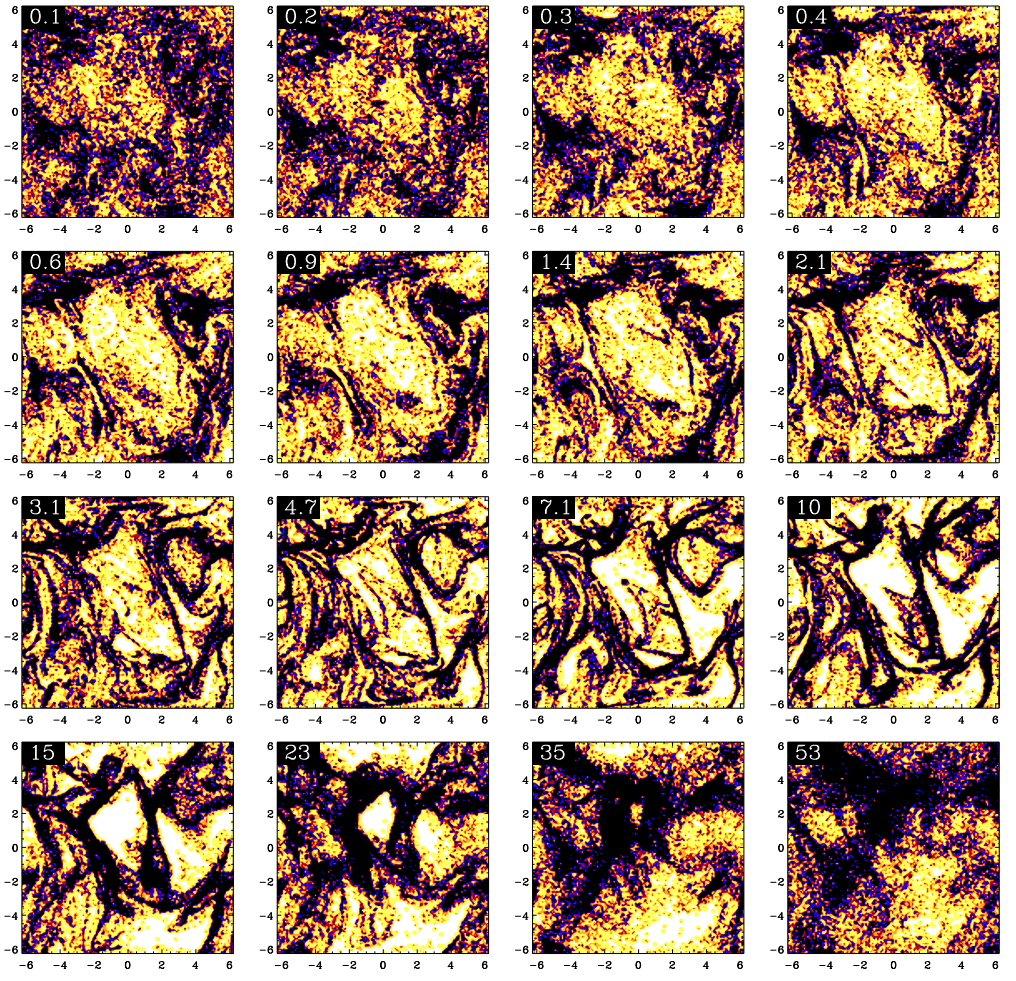

FIGURE 17. Similar to figure 7, but for Run C1.5 showing contour plots of particle number density for $St_{\rm int}$ in the range from 0.3 to 57.

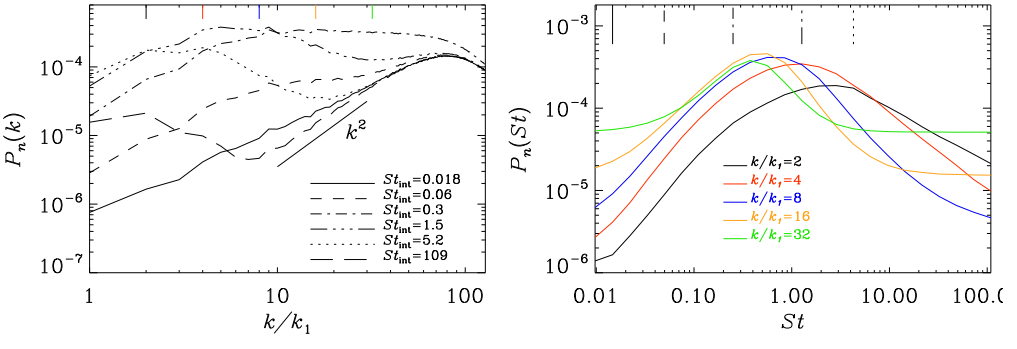

FIGURE 18. Similar to figure 14, but for Run V1 with more particle sizes.

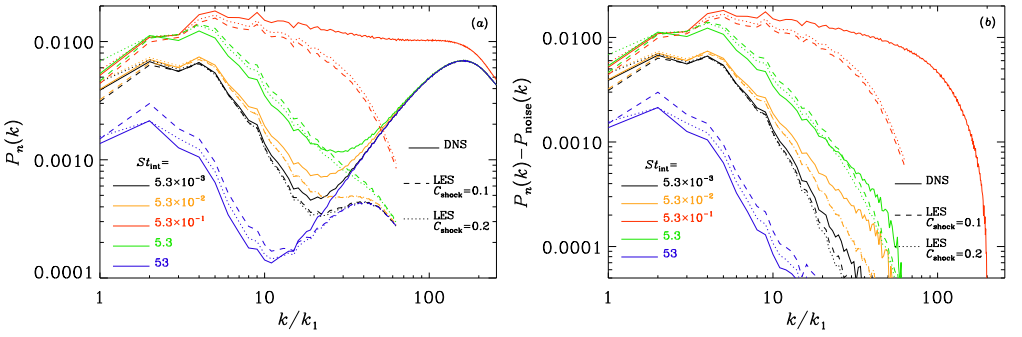

FIGURE 19. Comparison of Run V3a (solid lines), as well as Run V3s01 (dashed-dotted lines) and Run V3s02 (dotted lines) for (a) $P_n(k)$ and (b) $P_n(k) - P_{\rm noise}$.

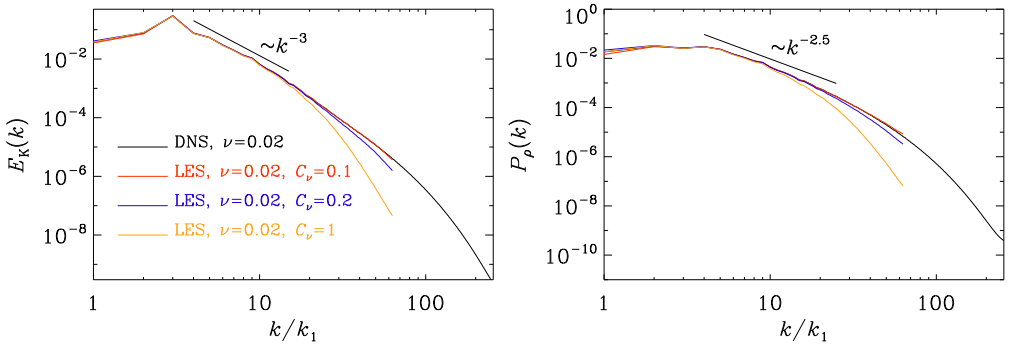

FIGURE 20. $E_{\rm K}(k)$ (left) and $P_\rho(k)$ (right) for Runs V3 and V3a (DNS with $\nu = 0.05$ and 0.02, respectively) as well as Runs V3s01, V3s02, and V3s1 (LES with $C_\nu = 0.1$, 0.2, and, 1 respectively).

Run	$\ell_{\rm Kol}$	δx	$\epsilon_{\rm K}$	Ma	Re
V1	0.042	0.049	0.0003	0.15	101
V2b	0.044	0.025	0.034	0.72	95
V3a	0.080	0.025	0.199	1.14	38
V3s01	0.074	0.098	0.267	1.15	38
V3s02	0.076	0.098	0.234	1.14	38
C2	0.213	0.049	0.064	0.74	15
C2a	0.107	0.025	0.061	0.76	38
C2s05	0.106	0.098	0.065	0.75	37
C2s1	0.106	0.098	0.063	0.74	37

TABLE 5. Summary of the Kolmogorov scale $\ell_{\rm Kol} = (\nu^3/\epsilon_{\rm K})^{1/4}$, mesh spacing δx, energy dissipation rate $\epsilon_{\rm K}$, as well as Mach and Reynolds numbers.

We should point out that the name LES is, in the present context, somewhat of a misnomer, because here all the eddies are actually resolved. This is because the Kolmogorov scale in Run V3 is about three times as large as the mesh spacing; see table 5. In the LES, the mesh spacing is four times larger than in the DNS, which means that we are resolving down to almost the Kolmogorov scale.

The quality of LES is worse for runs with compressive forcing; see figure 21, where we

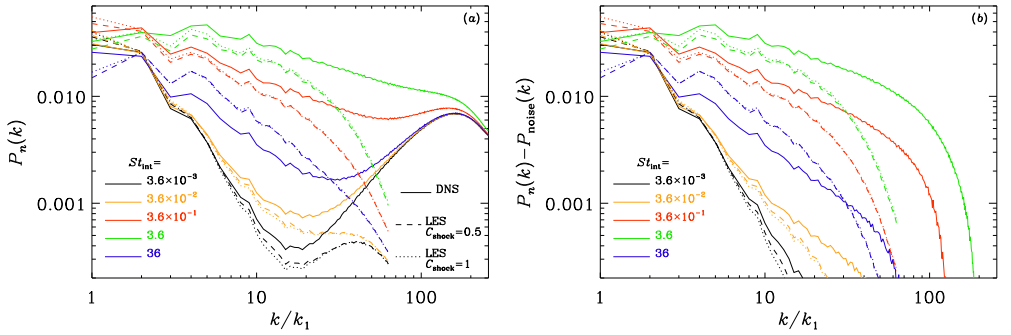

FIGURE 21. Comparison of Run C2 (solid lines), as well as Run C2s05 (dashed-dotted lines) and Run C2s1 (dotted lines) for (a) $P_n(k)$ and (b) $P_n(k) - P_{\text{noise}}$.

show the results for Run C2 with $Ma = 0.76$. We see that for $St_{\text{int}} = 3.6$ (green lines), the agreement between DNS and LES is rather poor even for small values of k/k_1. For $St_{\text{int}} = 0.36$ (red lines), the agreement is slightly better, but again only for small values of k/k_1.

5. Conclusions

In this work we have used particle power spectra to investigate particle clustering for compressible isotropic turbulence. We have studied the effect of using either the Epstein drag, which applies for $Kn \gg 1$, or the modified Stokesian drag, which applies for $Kn \ll 1$. As long as the particle radii are non-dimensionalised with the Stokes number, the power spectra resulting from the two drag laws turned out to be similar. This supports the general usefulness of the Stokes number – even for compressible flows and very diverse drag laws.

When using the concept of power spectra to analyse particle clustering of Lagrangian particles, it is important to realise that the number of particles used will have an effect on the power at large wavenumbers (small scales). This is due to the fact that, if too few particles are used, there are not enough particles to populate such small clusters and it becomes impossible to identify clusters at small scales. This effect is clearly seen through the presence of a k^2 contribution in the power spectra at small scales. The magnitude of the k^2 contribution is proportional to the inverse of the total number of particles in the simulation. If the Eulerian approach is used for the particles, it is implicitly assumed that an infinite number of particles are involved. This implies that the k^2 contribution to the power spectra is absent. However, this only applies to cases with an infinite number of particles.

When using the Eulerian particle approach, multi-valued particle velocities are not possible. This is because the Eulerian approach cannot represent caustics, which implies that only very small Stokes numbers would be modelled correctly. Furthermore, for larger Stokes numbers, artificial diffusion and viscosity must be used for the particle fluid in order to stabilise the simulations. This can yield nonphysical results. Hence, the Eulerian particle approach can only be used to simulate a very large number of particles that are small enough so that they behave almost as tracers.

We have seen significant differences in the clustering depending on how the turbulence is generated. For vortical forcing, the clustering peaks at an integral scale-based Stokes number of around unity. However, when we use compressive forcing, we drive strong flow divergences. In that case, we find that clustering peaks at two different Stokes numbers,

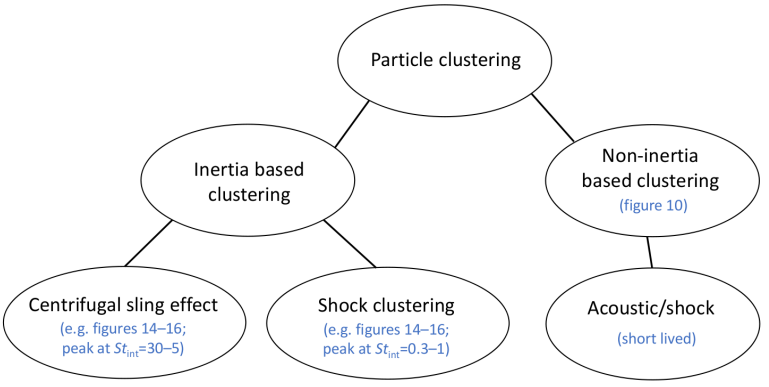

FIGURE 22. Sketch summarising the various clustering mechanisms discussed in this paper.

one somewhat below unity, and the other at much larger Stokes numbers. We argue that the first peak is explained by shock clustering, while the second is the usual Maxey-Riley clustering (based on the centrifugal sling effect), and its Stokes number is found to be around unity if it is evaluated based on the vortical part of the velocity field; see figure 22 for a summary.

In order to resolve shocks in high Mach number DNS, a very fine mesh is required. In many cases, interesting physics is, however, not related to the internal structure of the shocks themselves, but to the flows outside the shocks. It is therefore useful to model shocks through a shock viscosity instead of resolving them, such that a coarser mesh can be used. We investigated the effect on the particle clustering by using a shock-capturing viscosity to broaden the shocks. For the simulations performed here, the shock-broadening meant that the mesh was allowed to have four times less grid points in each direction. We found that the cases with shock-capturing viscosity reproduced the results of a fully resolved DNS for the first decade of wavenumbers rather accurately. However, the relatively strong clustering at small scales that was found for the DNS of particles with Stokes numbers slightly less than unity were not reproduced.

Acknowledgements

This work was supported by the Knut and Alice Wallenberg Foundation through the grant Dnr. KAW 2014.0048 on "Bottlenecks for particle growth in turbulent aerosols." We thank the Swedish Research Council, grant numbers 2015-04505 (ML) and 2019-04234 (AB), for partial financial support. The simulations were performed using resources provided by the Swedish National Infrastructure for Computing (SNIC) at the Royal Institute of Technology in Stockholm.

Code and data availability. The source code used for the simulations of this study, the PENCIL CODE (Pencil Code Collaboration *et al.* 2021), is freely available on `http://github.com/pencil-code/`. The DOI of the code is http://doi.org/10.5281/zenodo.2315093. The simulation setup and the corresponding data are freely available on `http://doi.org/10.5281/zenodo.4733175`; see also `http://www.nordita.org/~brandenb/projects/isoth_expwave/` for easier access.

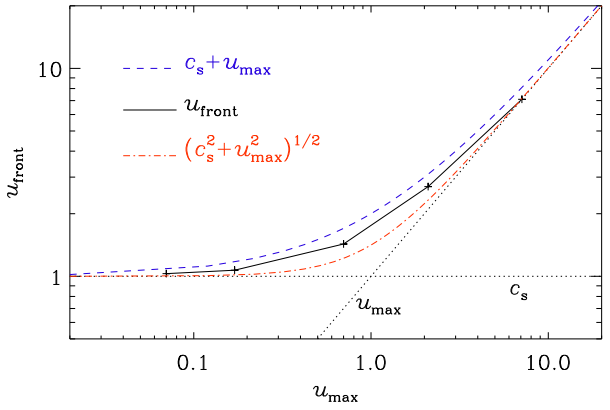

FIGURE 23. Front speed versus gas speed from the one-dimensional experiment described in the text (plus signs and black line), compared with the associated Doppler speed, $c_{\rm s} + u_{\rm max}$ (blue) and $(c_{\rm s}^2 + u_{\rm max}^2)^{1/2}$ (red).

Appendix A. Front speed versus gas speed

In Section 4.1.1, we used counter-propagating acoustic waves to drive inertial particles into each other. The speed of these waves is equal to the sound speed when the speed is small, but can become comparable to the gas speed for large velocities. This is shown in figure 23. Note that, even at subsonic gas speeds, the wave speed may exceed the speed of sound. Interestingly, the front speed is slightly faster than the associated Doppler speed, $c_{\rm s} + u_{\rm max}$, but slower than $(c_{\rm s}^2 + u_{\rm max}^2)^{1/2}$.

REFERENCES

BAKER, L., FRANKEL, A., MANI, A. & COLETTI, F. 2017 Coherent clusters of inertial particles in homogeneous turbulence. *J. Fluid Mech.* **833**, 364–398.

BEC, J. 2003 Fractal clustering of inertial particles in random flows. *Phys. Fluids* **15** (11), L81–L84, arXiv: nlin/0306049.

BEC, J., BIFERALE, L., CENCINI, M., LANOTTE, A., MUSACCHIO, S. & TOSCHI, F. 2007 Heavy Particle Concentration in Turbulence at Dissipative and Inertial Scales. *Phys. Rev. Lett.* **98** (8), 084502, arXiv: nlin/0608045.

BEC, J., BIFERALE, L., LANOTTE, A. S., SCAGLIARINI, A. & TOSCHI, F. 2010 Turbulent pair dispersion of inertial particles. *J. Fluid Mech.* **645**, 497, arXiv: 0904.2314.

BHATNAGAR, A., GUSTAVSSON, K. & MITRA, D. 2018 Statistics of the relative velocity of particles in turbulent flows: Monodisperse particles. *Phys. Rev. E* **97** (2), 023105, arXiv: 1710.04917.

BRANDENBURG, A. & DOBLER, W. 2002 Hydromagnetic turbulence in computer simulations. *Comp. Phys. Comm.* **147** (1-2), 471–475, arXiv: astro-ph/0111569.

CAUNT, S. E. & KORPI, M. J. 2001 A 3D MHD model of astrophysical flows: Algorithms, tests and parallelisation. *Astron. Astrophys.* **369**, 706–728, arXiv: astro-ph/0102068.

DE AVILLEZ, M. A. & BREITSCHWERDT, D. 2005 Global dynamical evolution of the ISM in star forming galaxies. I. High resolution 3D simulations: Effect of the magnetic field. *Astron. Astrophys.* **436** (2), 585–600, arXiv: astro-ph/0502327.

DEL SORDO, F. & BRANDENBURG, A. 2011 Vorticity production through rotation, shear, and baroclinicity. *Astron. Astrophys.* **528**, A145, arXiv: 1008.5281.

DRAINE, B. T. & SALPETER, E. E. 1979 Destruction mechanisms for interstellar dust. *ApJ* **231**, 438–455.

EATON, J. K. & FESSLER, J. R. 1994 Preferential concentration of particles by turbulence. *Int. J. Multiphase Flow* **20**, 169–209.

EVIRGEN, C. C., GENT, F. A., SHUKUROV, A., FLETCHER, A. & BUSHBY, P. J. 2019 The

supernova-regulated ISM - VI. Magnetic effects on the structure of the interstellar medium. *Mon. Not. Roy. Astron. Soc.* **488** (4), 5065–5074, arXiv: 1903.10263.

Federrath, C., Chabrier, G., Schober, J., Banerjee, R., Klessen, R. S. & Schleicher, D. R. G. 2011 Mach Number Dependence of Turbulent Magnetic Field Amplification: Solenoidal versus Compressive Flows. *Phys. Rev. Lett.* **107** (11), 114504, arXiv: 1109.1760.

Gent, F. A., Mac Low, M. M., Käpylä, M. J., Sarson, G. R. & Hollins, J. F. 2020 Modelling supernova-driven turbulence. *Geophys. Astrophys. Fluid Dynam.* **114** (1-2), 77–105, arXiv: 1806.01570.

Gent, F. A., Shukurov, A., Fletcher, A., Sarson, G. R. & Mantere, M. J. 2013*a* The supernova-regulated ISM - I. The multiphase structure. *Mon. Not. Roy. Astron. Soc.* **432** (2), 1396–1423, arXiv: 1204.3567.

Gent, F. A., Shukurov, A., Sarson, G. R., Fletcher, A. & Mantere, M. J. 2013*b* The supernova-regulated ISM - II. The mean magnetic field. *Mon. Not. Roy. Astron. Soc.* **430**, L40–L44, arXiv: 1206.6784.

Grabowski, W. W. & Wang, L.-P. 2013 Growth of Cloud Droplets in a Turbulent Environment. *Ann. Rev. Fluid Mech.* **45**, 293–324.

Gustavsson, K., Meneguz, E., Reeks, M. & Mehlig, B. 2012 Inertial-particle dynamics in turbulent flows: caustics, concentration fluctuations and random uncorrelated motion. *New J. Phys.* **14** (11), 115017, arXiv: 1206.2018.

Haugen, Nils Erland L., Brandenburg, Axel & Mee, Antony J. 2004 Mach number dependence of the onset of dynamo action. *Monthly Notices of the Royal Astronomical Society* **353** (3), 947–952, arXiv: https://academic.oup.com/mnras/article-pdf/353/3/947/4876625/353-3-947.pdf.

Haugen, N. E. L., Kleeorin, N., Rogachevskii, I. & Brandenburg, A. 2012 Detection of turbulent thermal diffusion of particles in numerical simulations. *Phys. Fluids* **24** (7), 075106–075106–16, arXiv: 1101.4188.

Haugen, N. E. L., Krüger, J., Mitra, D. & Løvås, T. 2018 The effect of turbulence on mass transfer rates of small inertial particles with surface reactions. *J. Fluid Mech.* **836**, 932–951.

Hopkins, P. F. & Lee, H. 2016 The fundamentally different dynamics of dust and gas in molecular clouds. *Mon. Not. Roy. Astron. Soc.* **456** (4), 4174–4190, arXiv: 1510.02477.

Johansen, A., Oishi, J. S., Mac Low, M.-M., Klahr, H., Henning, T. & Youdin, A. 2007 Rapid planetesimal formation in turbulent circumstellar disks. *Nature* **448** (7157), 1022–1025, arXiv: 0708.3890.

Johansen, A. & Youdin, A. 2007 Protoplanetary Disk Turbulence Driven by the Streaming Instability: Nonlinear Saturation and Particle Concentration. *Astrophys. J.* **662** (1), 627–641, arXiv: astro-ph/0702626.

Kadomtsev, B. B. & Petviashvili, V. I. 1973 Acoustic Turbulence. *Soviet Physics Doklady* **18**, 115.

Karchniwy, E., Klimanek, A. & Haugen, N. E. L. 2019 The effect of turbulence on mass transfer rates between inertial polydisperse particles and fluid. *J. Fluid Mech.* **874**, 1147–1168.

Korpi, M. J., Brandenburg, A., Shukurov, A., Tuominen, I. & Nordlund, Å. 1999 A Supernova-regulated Interstellar Medium: Simulations of the Turbulent Multiphase Medium. *ApJ* **514** (2), L99–L102.

Krüger, J., Haugen, N. E. L. & Lovas, T. 2017 Correlation effects between turbulence and the conversion rate of pulverized char particles. *Comb. Flame* **185**, 160–172.

Kwok, S. 1975 Radiation pressure on grains as a mechanism for mass loss in red giants. *ApJ* **198**, 583–591.

Mac Low, M.-M. & Klessen, R. S. 2004 Control of star formation by supersonic turbulence. *Rev. Mod. Phys.* **76** (1), 125–194, arXiv: astro-ph/0301093.

Mattsson, L., Bhatnagar, A., Gent, F. A. & Villarroel, B. 2019*a* Clustering and dynamic decoupling of dust grains in turbulent molecular clouds. *Mon. Not. Roy. Astron. Soc.* **483**, 5623–5641, arXiv: 1811.01082.

Mattsson, L., Fynbo, J. P. U. & Villarroel, B. 2019*b* Small-scale clustering of nano-dust grains in supersonic turbulence. *Mon. Not. Roy. Astron. Soc.* **490** (4), 5788–5797, arXiv: 1910.07289.

Maxey, M. R. 1987 The gravitational settling of aerosol particles in homogeneous turbulence and random flow fields. *J. Fluid Mech.* **174**, 441465.

Maxey, M. R. & Riley, J. J. 1983 Equation of motion for a small rigid sphere in a nonuniform flow. *Phys. Fluids* **26** (4), 883–889.

Mee, A. J. & Brandenburg, A. 2006 Turbulence from localized random expansion waves. *Mon. Not. Roy. Astron. Soc.* **370** (1), 415–419, arXiv: astro-ph/0602057.

Pencil Code Collaboration, Brandenburg, A., Johansen, A., Bourdin, P., Dobler, W., Lyra, W., Rheinhardt, M., Bingert, S., Haugen, N., Mee, A., Gent, F., Babkovskaia, N., Yang, C.-C., Heinemann, T., Dintrans, B., Mitra, D., Candelaresi, S., Warnecke, J., Käpylä, P., Schreiber, A., Chatterjee, P., Käpylä, M., Li, X.-Y., Krüger, J., Aarnes, J., Sarson, G., Oishi, J., Schober, J., Plasson, R., Sandin, C., Karchniwy, E., Rodrigues, L., Hubbard, A., Guerrero, G., Snodin, A., Losada, I., Pekkilä, J. & Qian, C. 2021 The Pencil Code, a modular MPI code for partial differential equations and particles: multipurpose and multiuser-maintained. *J. Open Source Software* **6** (58), 2807.

Porter, D. H., Jones, T. W. & Ryu, D. 2015 Vorticity, Shocks, and Magnetic Fields in Subsonic, ICM-like Turbulence. *Astrophys. J.* **810** (2), 93, arXiv: 1507.08737.

Schaaf, S. A. 1963 Mechanics of Rarefied Gases. *Handbuch der Physik* **3**, 591–624.

Shaw, R. A. 2003 Particle-Turbulence Interactions in Atmospheric Clouds. *Ann. Rev. Fluid Mech.* **35** (35), 183–227.

Squire, J. & Hopkins, P. F. 2017 The distribution of density in supersonic turbulence. *Mon. Not. Roy. Astron. Soc.* **471** (3), 3753–3767, arXiv: 1702.07731.

Squires, K. D. & Eaton, J. K. 1991 Preferential concentration of particles by turbulence. *Phys. Fluids A: Fluid Dynam.* **3** (5), 1169–1178, arXiv: https://doi.org/10.1063/1.858045.

von Neumann, J. & Richtmyer, R. D. 1950 A method for the numerical calculation of hydrodynamic shocks. *J. Appl. Phys.* **21**, 232–237.

Vosskuhle, M., Pumir, A., Lévêque, E. & Wilkinson, M. 2014 Prevalence of the sling effect for enhancing collision rates in turbulent suspensions. *J. Fluid Mech.* **749**, 841–852, arXiv: 1307.6853.

Weidenschilling, S. J. 1980 Dust to planetesimals: Settling and coagulation in the solar nebula. *Icarus* **44** (1), 172–189.

Wilkinson, M. & Mehlig, B. 2005 Caustics in turbulent aerosols. *Europhys. Lett.* **71** (2), 186–192, arXiv: cond-mat/0403011.

Yavuz, M. A., Kunnen, R. P. J., van Heijst, G. J. F. & Clercx, H. J. H. 2018 Extreme Small-Scale Clustering of Droplets in Turbulence Driven by Hydrodynamic Interactions. *Phys. Rev. Lett.* **120** (24), 244504.